

A DETAILED STUDY OF THE ACCRETION DISK SURROUNDING THE HIGH-MASS PROTOSTAR NGC 7538 S

GÖRAN SANDELL¹, MELVYN WRIGHT²

Accepted by ApJ

ABSTRACT

We present deep high angular resolution observations of the high-mass protostar NGC 7538 S, which is in the center of a cold dense cloud core with a radius of 0.5 pc and a mass of $\sim 2,000 M_{\odot}$. These observations show that NGC 7538 S is embedded in a compact elliptical core with a mass of 85 - 115 M_{\odot} . The star is surrounded by a rotating accretion disk, which powers a very young, hot molecular outflow approximately perpendicular to the rotating accretion disk. The accretion rate is very high, $\sim 1.4 - 2.8 \cdot 10^{-3} M_{\odot} \text{ yr}^{-1}$. Evidence for rotation of the disk surrounding the star is seen in all largely optically thin molecular tracers, $\text{H}^{13}\text{CN } J = 1 \rightarrow 0$, $\text{HN}^{13}\text{C } J = 1 \rightarrow 0$, $\text{H}^{13}\text{CO}^+ J = 1 \rightarrow 0$, and $\text{DCN } J = 3 \rightarrow 2$. Many molecules appear to be affected by the hot molecular outflow, including DCN and H^{13}CO^+ . The emission from CH_3CN , which has often been used to trace disk rotation in young high-mass stars, is dominated by the outflow, especially at higher K-levels. Our new high-angular resolution observations show that the rotationally supported part of the disk is smaller than we previously estimated. The enclosed mass of the inner, rotationally supported part of the disk ($D \sim 5''$, i.e. 14,000 AU) is $\sim 14 - 24 M_{\odot}$.

Subject headings: ISM: clouds – (stars:) circumstellar matter – stars: formation – stars: pre-main sequence – submillimeter

1. INTRODUCTION

How high-mass stars are formed is still under debate. High-mass stars are believed to form the same way as low mass stars, i.e. with a rotating accretion disk and driving an outflow, but in denser environments and with much higher accretion rates (Wolfire & Cassinelli 1987; Stahler et al. 2000; Norberg & Maeder 2000; McKee & Tan 2002; Keto 2003, 2007). However, others argue that high-mass stars are most likely formed by competitive accretion in a clustered environment (Bonnell & Bate 2006), or by adiabatic accretion of gas from the surrounding cluster to densities such that stellar collisions are likely to occur (Clarke & Bonnell 2008).

Accretion disks are ubiquitous in young low- and intermediate-mass stars, i.e. T Tauri and Herbig Ae stars (Simon, Dutrey & Guilloteau 2000; Mannings & Sargent 1997; Najita et al. 2003), which have sizes of one to a few hundred AU and appear to be in Keplerian rotation. Disks are also common in Class I objects, i.e. younger, more heavily embedded low- and intermediate mass pre-main-sequence stars (Brown & Chandler 1999), but there are very few examples of confirmed disks for the very earliest stages of a low-mass protostar, the Class 0 phase (Jørgensen 2004; Chandler et al. 2005). At the Class 0 phase, the temperature of the protostellar disk is of the same order of that of the collapsing cloud core, and it is therefore an observational challenge to get enough contrast between the disk and the cloud core.

The situation is even worse for high-mass stars, because they form in much denser environments and always in clusters or small groups. The survival time of

disks in high-mass stars is furthermore expected to be much shorter, because once the star is formed it will quickly photo evaporate the disk as soon as the accretion from the surrounding cloud starts to diminish, therefore allowing the uv-photons to reach the disk surface. Yet there are several detections of disks around early B-stars; Lkha 101 (Spectral class B0) (Tuthill et al. 2002), MWC297 (B1.5) (Manoj et al. 2007), MWC 349 A (B [e]) (Weintroub et al. 2008), clearly confirming that disks do exist around relatively massive stars.

Most young high-mass stars appear to drive outflows (Shepherd & Churchwell 1996; Zhang et al. 2001, 2005; Beuther et al. 2002b), but whether they also have accretion disks is less clear. There have been many reports of disks around high-mass stars, but only a few which appear well supported. Two of the most clearcut cases are IRAS 20126 + 4104 (Cesaroni et al. 1997, 1999, 2005; Zhang et al. 1998), and AFGL 490 (Schreyer et al. 2006). IRAS 20126 + 4104 has a luminosity of $\sim 1.3 \cdot 10^4 L_{\odot}$ suggesting an early B star. The star drives a parsec scale CO outflow (Wilking et al. 1990; Shepherd et al. 2000), and is surrounded by a rotating accretion disk with a diameter of $\sim 15,000 \text{ A.U.}$ (Cesaroni et al. 2005). The observed rotation curve for an edge-on Keplerian disk corresponds to $\sim 7 M_{\odot}$. The luminosity of AFGL 490, $L \sim 2 \cdot 10^3 L_{\odot}$ also suggests an early B-star. It drives a more compact outflow, 0.3 pc (corrected for inclination) (Lada & Harvey 1981; Snell et al. 1984) and is surrounded by a nearly face-on disk with a radius $\sim 1600 \text{ AU}$, which has a disk mass of $1 M_{\odot}$ and appears to be in Keplerian rotation (Schreyer et al. 2006). Another, even younger high-mass protostar, NGC 7538 S, with a luminosity of $\sim 1.5 \cdot 10^4 L_{\odot}$, which is surrounded by a large, nearly edge-on disk with a radius of 15,000 AU and a disk mass of $\sim 100 M_{\odot}$ was reported by Sandell, Wright & Forster (2003). The disk drives a compact molecular outflow with a size of

Goran.H.Sandell@nasa.gov

¹ SOFIA-USRA, NASA Ames Research Center, MS N211-3, Moffett Field, CA 94035, USA

² Radio Astronomy Laboratory, University of California, Berkeley, 601 Campbell Hall, Berkeley, CA 94720, USA

0.1 - 0.4 pc and shows a Keplerian-like rotation.

This disk is the target for our studies. In this paper we present follow-up BIMA spectral line observations of several molecules in the 3 and 1 mm bands, which were chosen to measure the rotation of the disk surrounding NGC 7538 S. In a companion paper (Corder et al., in preparation; hereafter Paper II) we discuss high-angular resolution continuum observations of NGC 7538 S and the Ultra-Compact H II regions NGC 7538 IRS 1 - 3 with BIMA, CARMA, and the VLA, which provide us with better mass estimates of the disk/envelope surrounding the star.

2. OBSERVATIONS AND DATA REDUCTION

2.1. BIMA array observations

Between 2002 and 2004 we obtained more observations on NGC 7538 S with the BIMA array at 86 and 89 GHz. These observations are summarized in Table 1. At 3.4 mm (87 GHz) we combined additional data obtained in the B, C and D array configurations with the data reported by (Sandell, Wright & Forster 2003) to produce deep high fidelity maps in H^{13}CN $J=1\rightarrow 0$, HCO^+ $J=1\rightarrow 0$, SO $2_2 \rightarrow 1_1$ and NH_2D $1_{11} \rightarrow 1_{01}$. We also improved the H^{13}CO^+ $J=1\rightarrow 0$, HN^{13}C $J=1\rightarrow 0$, and SiO $J=2\rightarrow 1$, by adding a B-array track to the existing C-array data. All these observations use the same correlator setup and were reduced as described in Sandell, Wright & Forster (2003).

Table 2 summarizes the spectral line observations at 1.4 mm (220 GHz), which we obtained with BIMA during the same time frame as the 3.4 mm observations. These 1.4 mm observations were obtained in the B and C configurations, and provide similar angular resolution as the 87 GHz data sets. In this paper we discuss the results from DCN $J=3\rightarrow 2$ and CH_3CN $J=12\rightarrow 11$ ($K=0$ to 5), which were expected to be optically thin and hence good tracers of the accretion disk. Our observations also included SO $J=5_5\rightarrow 4_4$, H_2CO $3_{03}\rightarrow 2_{02}$ and $3_{22}\rightarrow 2_{21}$, and ^{13}CO $J=2\rightarrow 1$ (Table 2), but the lines are optically thick and self-absorbed and do not provide us any information on the deeply embedded accretion disk. We therefore leave the discussion of these lines to a later paper.

The 1 mm data were reduced and imaged in a standard way using MIRIAD software (Sault, Teuben & Wright 1995). The quasar 0102+584 was used as phase calibrator and Mars and/or 3C84 for passband and flux calibration. The uncertainty in the absolute amplitude scale is $\sim 20\%$ at 1.4 mm, but the relative amplitude of the spectral lines observed simultaneously is $\sim 5\%$.

The BIMA array, like every interferometer, will filter out extended, relatively uniform emission, resulting in an underestimate the total emission (missing flux). Furthermore, extended emission will cause negative features in the spectra, which may look like self-absorption. Since we expect to see self-absorption if the protostellar disk is warmer than the surrounding cloud, it becomes difficult, if not impossible, to judge what features are real, and what are artifacts, unless we fill in missing short uv-spacings. We therefore carried out observations with FCRAO at 3.4 mm band and with JCMT at 1.4 mm to provide missing short spacings for several key molecules.

2.2. FCRAO observations

TABLE 1
BIMA 3 MM OBSERVING LOG.

Molecule	transition	rest frequency [GHz]
Frequency setting: H^{13}CN $J=1\rightarrow 0$; Array configurations BCD,		
HPBW = $6''.0 \times 5''.7$ pa = -25.8°		
Observing dates: 01/27/02, 01/31/02, 05/03/02, 08/09/03,		
11/04/03, 12/11/03 12/12/03, 12/31/03		
NH_2D	$1_{11} \rightarrow 1_{01}$ $F' - F'' = 0 - 1$	85.924747
NH_2D	$1_{11} \rightarrow 1_{01}$ $F' - F'' = 2 - 1$	85.925684
NH_2D	$1_{11} \rightarrow 1_{01}$ $F' - F'' = 2 - 2/1 - 1$	85.926263
NH_2D	$1_{11} \rightarrow 1_{01}$ $F' - F'' = 1 - 2$	85.926858
NH_2D	$1_{11} \rightarrow 1_{01}$ $F' - F'' = 1 - 0$	85.927721
SO	$J=2, 2\rightarrow 1, 1$	86.09355
H^{13}CN	$J=1\rightarrow 0$ $F = 1 - 1$	86.338767
H^{13}CN	$J=1\rightarrow 0$ $F = 2 - 1$	86.340184
H^{13}CN	$J=1\rightarrow 0$ $F = 0 - 1$	86.342274
HCO^+	$J=1\rightarrow 0$	89.188518

Frequency setting: H^{13}CO^+ $J=1\rightarrow 0$; Array configurations BC,

HPBW = $7''.9 \times 6''.9$ pa = -23.8°

Observing dates: 12/03/01, 01/10/04

H^{13}CO^+	$J=1\rightarrow 0$	86.754294
SiO	$J=2\rightarrow 1$ $v=0$	86.846998
HN^{13}C	$J=1\rightarrow 0$ $F = 0 - 1$	87.090735
HN^{13}C	$J=1\rightarrow 0$ $F = 2 - 1$	87.090859
HN^{13}C	$J=1\rightarrow 0$ $F = 1 - 1$	87.090942

TABLE 2
BIMA 1 MM OBSERVING LOG.

Molecule	transition	rest frequency [GHz]
Frequency setting: H_2CO $3_{03}\rightarrow 2_{02}$; array configurations: BC		
HPBW = $6''.6 \times 5''.7$ pa = 78.4°		
Observing dates: 10/9/02, 10/16/02		
SO	$J=5, 5\rightarrow 4, 4$	215.22065
H_2CO	$3_{03}\rightarrow 2_{02}$	218.22219
H_2CO	$3_{22}\rightarrow 2_{21}$	218.47564

Frequency setting: DCN $J=3\rightarrow 2$; array configurations: BC

HPBW = $2''.9 \times 2''.4$ pa = 22.2°

Observing dates: 10/13/02, 04/19/03, 05/01/03, 10/10/03,

10/25/03, 01/03/04, 01/05/04

DCN	$J=3\rightarrow 2$	217.23853
^{13}CO	$J=2\rightarrow 1$	220.39869
CH_3CN	$12_0 \rightarrow 11_0$	220.74727
CH_3CN	$12_1 \rightarrow 11_1$	220.74302
CH_3CN	$12_2 \rightarrow 11_2$	220.73027
CH_3CN	$12_3 \rightarrow 11_3$	220.70903
CH_3CN	$12_4 \rightarrow 11_4$	220.6793
CH_3CN	$12_5 \rightarrow 11_5$	220.64109
CH_3CN	$12_6 \rightarrow 11_6$	220.59443
$\text{CH}_3^{13}\text{CN}$	$12_2 \rightarrow 11_2$	220.62108
$\text{CH}_3^{13}\text{CN}$	$12_3 \rightarrow 11_3$	220.59994

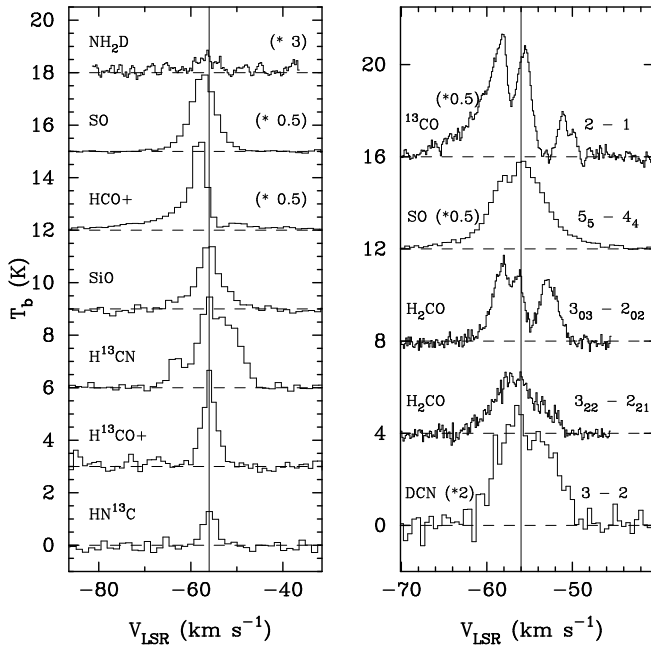


FIG. 1.— Spectra toward NGC 7538 S at 3 mm (left panel) and 1 mm (right panel). Spectra for HCO^+ and H^{13}CN in the 3 mm window and for ^{13}CO and H_2CO in the 1 mm window are BIMA data merged with single dish data to correct for missing zero-spacings. The red-shifted self-absorption we see in these molecular transitions is therefore real and not due to missing flux filtered out by the interferometer. The grey vertical line marks the systemic velocity. In the 3 mm window HCO^+ , SiO and SO show strong line wings; both SO and HCO^+ are self-absorbed at red-shifted velocities. At 1 mm all the spectra shown here exhibit line wings. ^{13}CO $J=2\rightarrow 1$ and H_2CO $3_{03}\rightarrow 2_{02}$ show deep self-absorption at red-shifted velocities. Even DCN $J=3\rightarrow 2$ is affected by some red-shifted self-absorption. The scaling factor is shown in parenthesis.

The observations were carried out on November 9, 2004 by Dr. Mark Heyer with the 14-m Five College Radio Astronomy Observatory (FCRAO) telescope using the SEQUOIA 16 beam array receiver. The weather conditions were excellent, resulting in a system temperature, $T_{\text{sys}} \sim 120$ K. We used the dual channel correlator (DCC) with a 50 MHz bandwidth and a spectral resolution of 48.8 kHz (0.16 km s^{-1}). The DCC was configured to simultaneously cover H^{13}CN $J=1\rightarrow 0$ and HCO^+ $J=1\rightarrow 0$. At 86 and 89 GHz the half-power beam width (HPBW) is $58''$ and $57''$, respectively, while the main-beam efficiency, $\eta_{\text{mb}} \sim 0.50$. The observations were performed using on-the-fly (OTF) mapping, covering a $9' \times 9'$ area centered at $\alpha_{2000.0} = 23^{\text{h}} 13^{\text{m}} 45^{\text{s}}.4$, $\delta_{2000.0} = +61^{\circ} 28' 10''.5$, and covering the whole molecular cloud associated with NGC 7538. The OTF maps were re-gridded to a cell size $20''$. Both data sets were merged with our BIMA data using the MIRIAD task IMMERGE and assuming the HPBWs and efficiencies for FCRAO quoted above. The single dish and interferometer data were compared in the Fourier domain in a range of overlapping spatial frequencies corresponding to 6-10m to align the flux calibration scales.

2.3. JCMT observations

Complementary single dish observations (projects m04ai09 and m05ai07) were carried out in service mode

on the James Clerk Maxwell Telescope (JCMT)³ on Mauna Kea, Hawaii, between April 2004 and May 2005. With JCMT we obtained fully sampled maps of DCN $J=3\rightarrow 2$, H_2CO $3_{03}\rightarrow 2_{02}$ and $3_{22}\rightarrow 2_{21}$, ^{13}CO $J=2\rightarrow 1$, and C^{18}O $J=2\rightarrow 1$, as well as long integration (10 - 30 min) single spectra at the center position (NGC 7538 S). We also took deep (long integration) spectra of ^{12}CO and C^{17}O $J=2\rightarrow 1$. All these observations used receiver RxA3, a single beam SiS mixer covering the 1.3 mm spectral window. At 217 GHz the measured HPBW is $22''.3$ and the main beam efficiency, $\eta_{\text{mb}} = 0.70$. All maps were made in OTF-mode with heavy oversampling; $5''$ sampling interval with an integration time of 5 second per resolution element. The maps have a size $55'' \times 45''$. We used the Digital Autocorrelator Spectrometer (DAS) with 125 MHz bandwidth (^{13}CO and C^{18}O) or 250 MHz bandwidth (DCN, H_2CO) providing us with spectral resolutions 78.1 kHz and 156.2 kHz, respectively. Most of the observing was in wet weather conditions, resulting in system temperatures, T_{sys} of 400 - 450 K. The receiver calibration was regularly checked on planets (Uranus or Mars) and we always took reference spectra on NGC 7538 IRS 1.

Our DCN setup also included the SiO $J=4\rightarrow 3$ transition at 217.10494 GHz. In total we acquired 10 maps, because the line is rather faint. Some scans had poor baseline stability and had to be thrown out, and for most of the observations we had to use high order polynomials for baseline subtraction. During the data reduction we discovered an additional line in our spectra, which we identified as the SO_2 $13_{2,12}\rightarrow 13_{1,13}$ at 225.153689 GHz, i.e. in the upper sideband. SiO and SO_2 show broad line wings, indicating that the emission is strongly affected by the outflow. The DCN-map shows that the emission is rather compact with a size $\sim 30''$. When we add it to the BIMA data, we do not see any changes in the morphology of the DCN emission. However, since the combined map had poorer signal to noise due to insufficient integration time, we make use of only the high-angular resolution BIMA map in this paper.

Both H_2CO transitions were observed simultaneously. We obtained three maps with good quality. The coadded map matched well the noise level in our BIMA data. At ^{13}CO $J=2\rightarrow 1$ we obtained a total of 7 maps, largely because we needed good SNR on the faint wings from the outflow. The coadded map was of very good quality and was successfully added to our BIMA data on ^{13}CO . For C^{18}O $J=2\rightarrow 1$ we obtained 4 maps, also of good quality. Since we never mapped NGC 7538 S with BIMA in C^{18}O , we have used this map stand-alone to look at the large scale morphology of the cloud core.

3. RESULTS AND ANALYSIS

In Figure 1 we show spectra towards NGC 7538 S of all the molecular transitions, which have been observed with BIMA in the 3 mm and 1 mm band, except the CH_3CN $J=11\rightarrow 10$ lines, which we will cover in Section 3.4.3. Although some of the changes in the line profiles are due to different spatial resolution, this effect is rather mi-

³ The JCMT is operated by the Joint Astronomy Centre, on behalf of the UK Particle Physics and Astronomy Research Council, the Netherlands Organization for Scientific Research, and the Canadian National Research Council.

TABLE 3
 GAUSSIAN FITS WITH CLASS OF OPTICALLY THIN OR MODERATELY OPTICALLY THIN
 LINES TOWARDS THE CENTER OF THE ACCRETION DISK, $\alpha_{2000.0} = 23^h 13^m 44^s.98$,
 $\delta_{2000.0} = +61^\circ 26' 49''.7$.

Molecule	Transition	HPBW [" × "]	$\int T_{\text{MB}} dV$ [K km s ⁻¹]	ΔV [km s ⁻¹]	V_{LSR} [km s ⁻¹]
C ¹⁸ O _a	2 → 1	21.6 × 21.6	33.44 ± 0.21 −1.22 ± 0.11	4.68 ± 0.03 2.10 ± 0.20	−56.42 ± 0.01 −55.73 ± 0.11
C ¹⁷ O	2 → 1	21.2 × 21.2	9.53 ± 0.03	5.04 ± 0.18	−56.42 ± 0.02
H ¹³ CO ⁺	1 → 0	7.9 × 6.9	14.73 ± 1.00	4.20 ± 0.36	−55.96 ± 0.14
HN ¹³ C ^b	1 → 0	7.8 × 7.1	5.40 ± 0.17	3.60 ± 0.10	−55.91 ± 0.36
SiO ^c	2 → 1	8.2 × 7.1	7.85 ± 0.90	3.73 ± 0.33	−56.23 ± 0.13
H ¹³ CN ^{d,e}	1 → 0	5.8 × 5.7	37.00 ± 0.70	4.70 ± 0.10	−56.20 ± 0.13
H ¹³ CN ^f	1 → 0	4.0 × 3.7	24.86 ± 0.22	5.85 ± 0.05	−55.97 ± 0.12
NH ₂ D ^f	1 ₁₁ → 1 ₀₁	12.1 × 11.9	5.30 ± 0.06	1.35 ± 0.10	−56.28 ± 0.06
DCN _a	3 → 2	2.9 × 2.4	21.69 ± 0.84 −2.88 ± 0.70	6.89 ± 0.18 2.65 ± 0.01	−55.56 ± 0.18 −54.85 ± 0.21

^a Fit to self-absorption component

^b ΔV and V_{LSR} from method hfs in CLASS, see Section 3.

^c This is the cloud component only. SiO is dominated by high velocity emission, which has a line integral of 16.6 K km s⁻¹ and a line width of 13.6 km s⁻¹.

^d Single dish corrected spectrum

^e Fit with hyperfine components locked in velocity separation to the main hyperfine line.

^f High spatial resolution BIMA spectrum; V_{LSR} from method hfs.

nor, especially since most of the spectral lines have been observed with roughly the same angular resolution (Table 1 & 2). Most of the differences in line shape results from whether the lines are optically thick or thin, and whether they originate from the disk, the outflow, or the cloud envelope. Almost all the lines observed in the 1 mm band are optically thick, have strong line wings, and show deep self-absorption from the surrounding cloud envelope. The same is also true for HCO⁺ J=1→0, SiO J=2→1, and SO J=2,2→1,1 in the 3 mm band. In this paper we are focusing on the accretion disk. We therefore limit our analysis to high density tracers, which have dipole moments of 3 Debye or larger, and which can be assumed to be optically thin or at least have only moderate optical depths. Of the molecules we have observed, H¹³CN, HN¹³C, DCN, H¹³CO⁺, CH₃¹³CN, and CH₃CN, all fall into this category. These molecules are expected to be good tracers of the gas in the dense disk surrounding NGC 7538 S. Most of them are isotopomers, which have molecular abundance ratios of $\lesssim 10^{-10}$ compared to H₂. One would therefore expect them to be optically thin, but as we will see later, this is not the case for all of the lines. Several of them are also affected by emission from the molecular outflow. We have therefore carefully inspected each image to see whether the line emission originates from the disk, the outflow, or whether both the disk and the outflow contribute to the emission. The gas in the surrounding cloud core is also very dense, and colder than the gas in the disk. It can therefore absorb some of the emission from the disk. However, since the surrounding envelope is much more extended than the disk and relatively uniform, it is largely filtered out in these interferometer observations, but may nevertheless add some contribution to the line profiles observed towards the accretion disk.

In order to determine the systemic velocity of the disk, we extracted spectra from our BIMA images for all optically thin or moderately optically thin molecules (see

Table 3) at the center of the accretion disk. These spectra were imported into the IRAM single dish spectral line reduction package CLASS, which is part of the GILDAS software suite⁴. CLASS has very good line fitting routines and can also handle molecules with hyperfine splitting. The “method hfs” allows fitting for optical depth of lines with hyperfine structure, and one can derive more accurate radial velocities by locking the velocity separation for satellite lines to the main emission component as long as all the spectral transitions are observed within a single band. We also fitted deep, single dish JCMT spectra of the CO isotopomers C¹⁸O, and C¹⁷O J=2→1 to determine the systemic velocity of the cloud. The results of these Gaussian fits are given in Table 3. C¹⁸O J=2→1 and DCN J=3→2 show a narrow self-absorption feature at the cloud velocity or at slightly red-shifted velocities, suggesting that both have an optical depth of at least one in the surrounding cloud core. H¹³CN J=1→0 shows evidence for self-absorption in the main hyperfine component at high angular resolutions, see Section 3.4.1. Even C¹⁷O J=2→1 shows a weak hint of self-absorption and a fit to the hyperfine splitting of the molecule (method hfs) gives an optical depth $\tau \sim 0.25$. The results from Table 3 suggest a systemic velocity of -56.0 ± 0.2 km s⁻¹. This agrees very well with what we derive from the rotation curve of H¹³CN J=1→0, while the DCN rotation curve would suggest a slightly more red-shifted systemic velocity, -55.7 km s⁻¹.

3.1. The NGC 7538 S star forming cloud core

The NGC 7538 S star forming core is a cold, dense cloud core $\sim 80''$ south of NGC 7538 IRS 1 (Werner et al. 1979; Zheng et al. 2001; Sandell & Sievers 2004). Here we have assumed a distance of 2.8 kpc for easy comparison with earlier work, although recent trigonometric parallax observations (Moscadelli et al. 2009), result in a

⁴ <http://www.iram.fr/IRAMFR/GILDAS>

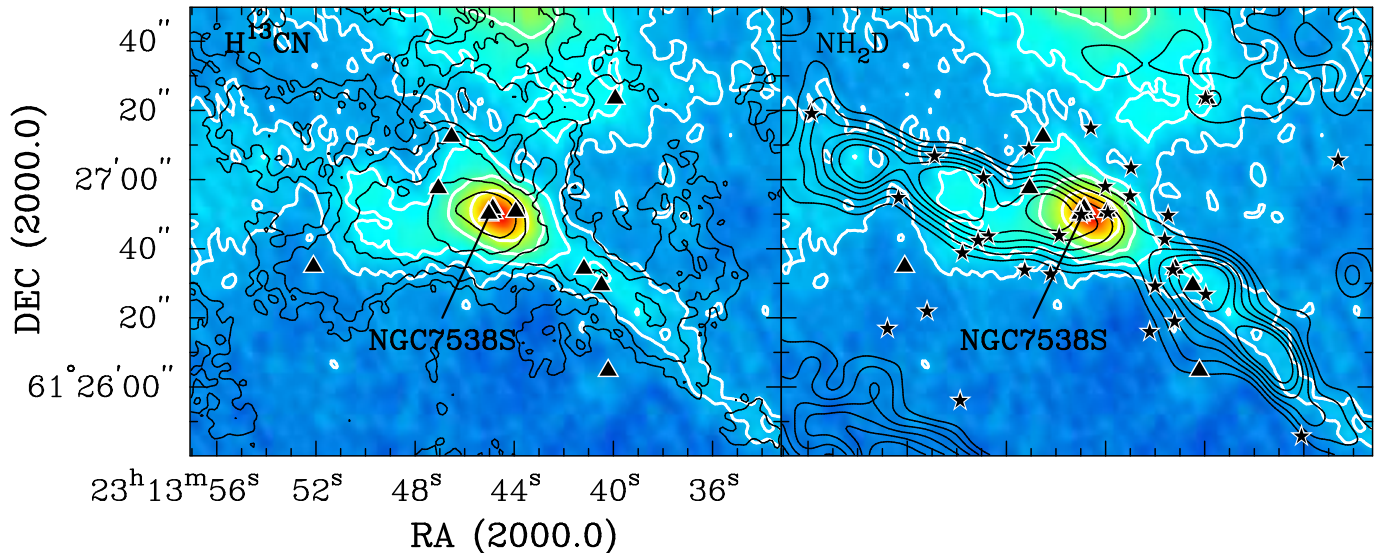


FIG. 2.— Contour plots of total integrated H^{13}CN $J=1\rightarrow 0$ emission (left panel) and of the NH_2D $1_{11} \rightarrow 1_{01}$ emission (right panel) overlaid on a color image of the $450\ \mu\text{m}$ continuum emission. The $450\ \mu\text{m}$ map is taken from Sandell & Sievers (2004). It has been cleaned and restored with a $10''$ circular beam to better bring out the faint low level dust emission. The peak flux of the $450\ \mu\text{m}$ emission is $77.3\ \text{Jy beam}^{-1}$. In order to better see the low level emission we have enhanced the color image with four thick white contours plotted logarithmically from $4\ \text{Jy beam}^{-1}$ to half intensity. The H^{13}CN emission is plotted with six logarithmic black contours, starting at $28\ \text{mJy beam}^{-1}$ ($3\text{-}\sigma$) to peak intensity, $590\ \text{mJy beam}^{-1}$. For NH_2D we use an image with $12''$ resolution. The contours for this image are plotted with six black logarithmic contours going from $9\ \text{mJy beam}^{-1}$ ($3\text{-}\sigma$) to peak intensity, $120\ \text{mJy beam}^{-1}$. We have overlaid the images with H_2O masers (black triangles) and IRAC $8\ \mu\text{m}$ sources (black star symbols) (Paper II), which pinpoint the location of young stars in this region. We have also labeled the position of NGC 7538 S.

slightly smaller distance, $2.65 \pm 0.12\ \text{kpc}$. The star forming core has a luminosity of $\sim 10^4\ L_{\odot}$ and harbors at least one massive protostar, NGC 7538 S (Sandell, Wright & Forster 2003). Zheng et al. (2001), who mapped the NGC 7538 molecular cloud in NH_3 with the VLA at high angular resolution, found the strongest ammonia emission towards NGC 7538 S, in good agreement with the sub-mm continuum imaging by Sandell & Sievers (2004). In the vicinity of NGC 7538 S Zheng et al. found the NH_3 emission to be optically thick with a temperature of $\sim 25\ \text{K}$.

Our H^{13}CN $J=1\rightarrow 0$ map with FCRAO and BIMA is in good agreement with the dust continuum and the NH_3 results. Overall we find H^{13}CN to show the same cloud morphology as the dust continuum. This is shown in Figure 2, where we overlaid the integrated H^{13}CN emission from our combined FCRAO and BIMA map on the $450\ \mu\text{m}$ SCUBA continuum map from Sandell & Sievers (2004) for the region around NGC 7538 S. The dust continuum and the H^{13}CN emission both peak on NGC 7538 S and the narrow south-western filament shows up clearly in both images. The dust emission appears somewhat more extended than H^{13}CN to the east of NGC 7538 S, and there are also some differences to the north, i.e. the southernmost part of the NGC 7538 IRS 1 cloud core. Most of these differences are most likely due to difference in temperature of the emitting gas and dust. Since Zheng et al. (2001) found very strong, cold NH_3 emission towards NGC 7538 S, we decided to look for NH_2D emission as well, which we could observe with the same frequency setup as H^{13}CN and HCO^+ (Section 2.1, Table 1). The NH_2D emission is quite faint, especially towards NGC 7538 S, but the narrow, lumpy, southwestern filament shows up very well in the integrated NH_2D emission (Figure 2b). However, the NH_2D emission is

even stronger to the east of NGC 7538 S, where it shows a “continuation” of the southwestern filament, which is not evident in dust continuum, nor is it seen in H^{13}CN or any other of the molecules that we have imaged towards NGC 7538 S. Examination of NH_2D spectra along the filaments show broadened lines at the positions of the knots in the filaments and sudden, small velocity shifts between the knots, suggesting that these “clumps” maybe gravitationally unstable and that they may already have formed stars. The only exception is the NH_2D clump at the tip of the eastern filament. This is where we find the strongest NH_2D emission, but the lines are very narrow ($\Delta v = 0.9\ \text{km s}^{-1}$), suggesting that this condensation is a very cold, prestellar core.

We can use our high-quality spectral line and continuum data to estimate the size and total mass of the NGC 7538 S star forming core. Sandell & Sievers (2004) quoted a radius of $0.4\ \text{pc}$ ($30''$) and a total mass of $750\ M_{\odot}$, assuming an average dust temperature of $30\ \text{K}$. If we use our combined FCRAO and BIMA H^{13}CN map and radially average the data from the center of the protostar, we find that the emission is relatively flat at small radii, has a steeper fall-off to a radius of $\sim 18 - 20''$ and gets even steeper at larger radii until it flattens off at $\sim 38''$ from the cloud center. The emission stays roughly constant at larger radii until it start to rise again when we pick up emission from the IRS 1 core. If we radially average the $450\ \mu\text{m}$ map (Figure 2), we find a core size of $34''$. The $850\ \mu\text{m}$ image, however, has better sensitivity than the $450\ \mu\text{m}$ -map, and here the radially averaged dust emission suggests a core radius of $\sim 40''$, which agrees well with H^{13}CN after correcting for the difference in HPBW. The dust emission therefore has a similar distribution to H^{13}CN , although it falls off less steeply at larger radii, see Figure 3. Both dust and gas therefore

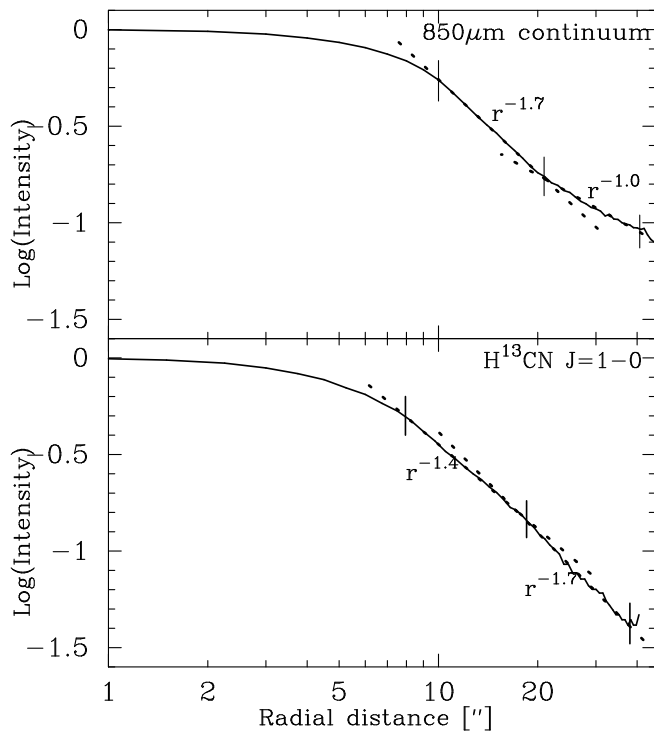


FIG. 3.— Radially averaged intensity profiles (normalized to one) of $\text{H}^{13}\text{CN } J=1 \rightarrow 0$ and the $850 \mu\text{m}$ SCUBA image centered on NGC 7538 S. The distribution of both H^{13}CN and dust emission is relatively flat at small radii ($r < 8''$). Between $8''$ and $20''$ the falloff in density is proportional to $r^{-\alpha}$, where α is in the range 1.4 - 1.7. At larger radii H^{13}CN falls off steeper, while the dust emission flattens out. Both H^{13}CN and the dust emission indicate a core size of $\sim 38''$. The break points between different regimes are shown by vertical lines in both plots.

predict a core radius of $\sim 0.5 \text{ pc}$ ($38''$). If we assume an average gas temperature of 25 K, consistent with the temperature derived from NH_3 , and an abundance ratio for H^{13}CN similar to the OMC-1 extended ridge (Blake et al. 1987), i.e. $[\text{HCN}]/[\text{H}_2] = 5 \times 10^{-9}$, and an isotope ratio⁵ $^{12}\text{CO}/^{13}\text{CO} = 40$, we obtain a total mass of $\sim 2,000 M_{\odot}$.

As discussed above the core size is the same for the dust emission as found for H^{13}CN , even though there are differences in the morphology on smaller scales. If we assume that the gas and dust is thermalized at 25 K, and take a β -index of 1.5, the SCUBA maps give a total mass of $\sim 2,000 M_{\odot}$, which is in excellent agreement with H^{13}CN . The JCMT $\text{C}^{18}\text{O } J=2 \rightarrow 1$ map, however, gives a mass of only $\sim 1,000 M_{\odot}$, if we assume that C^{18}O is optically thin. We know that this assumption is not true near the core center, and the total mass will therefore be somewhat underestimated. However, the main reason for low mass derived from CO is that a large fraction of the CO is frozen onto dust grains, resulting in a depletion of the CO gas phase abundance. Mitchell et al. (1990) found $\sim 10\%$ of the CO to be tied up into ice in the NGC 7538 IRS 9 cloud core. Since the NGC 7538 S cloud

⁵ The $^{12}\text{C}/^{13}\text{C}$ abundance is strongly fractionated in cold cloud cores and ~ 40 throughout OMC-1, see e.g. Blake et al. (1987). It therefore appears more appropriate to use this isotope ratio for the NGC 7538 molecular cloud, rather than 85, which was used by Sandell, Goss & Wright (2005) in their study of the IRS 9 cloud core. The observed $^{12}\text{CO}/^{13}\text{CO}$ ratios at high velocities suggest that the isotope ratio could be slightly higher, ~ 60 .

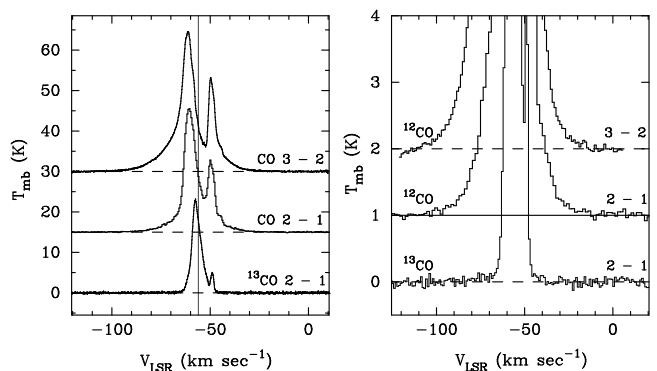


FIG. 4.— Left panel: Long integration single dish (JCMT) spectra of $\text{CO } J=2 \rightarrow 1$, $J=3 \rightarrow 2$, and $^{13}\text{CO } J=2 \rightarrow 1$. The red-shifted emission peak at $\sim -49 \text{ km s}^{-1}$ is due to an extended cloud unrelated to the outflow. The systemic velocity at -56 km s^{-1} is marked with a vertical line. Right panel: The same spectra binned over 6 or 8 channels and plotted to show the faint high velocity emission.

core is even colder than the IRS 9 cloud, the fraction of solid to gas phase CO is likely to be higher. The low core mass deduced from C^{18}O is therefore a result of CO depletion and optical depth. We therefore conclude that the total mass of the NGC 7538 S cloud core is $\sim 2,000 M_{\odot}$, corresponding to an average gas density of $\sim 6 \times 10^4 \text{ cm}^{-3}$.

3.2. The position of the central protostar, NGC 7538 S

NGC 7538 S was detected in deep IRAC images with the *Spitzer* Space Observatory at 4.5, 5.8, and $8 \mu\text{m}$ (Paper II). In paper II we also present VLA observations, which show that the star drives a highly collimated thermal jet, with the strongest emission knot coinciding with the IRAC position to within $0''.1$. In this paper we have therefore adopted the VLA position of NGC 7538 S as: $\alpha_{2000.0} = 23^{\text{h}} 13^{\text{m}} 44^{\text{s}}.98$, $\delta_{2000.0} = +61^{\circ} 26' 49''.7$ ⁶. This position coincides within errors with the strongest OH maser spots (Argon et al. 2000), the position of the Class II CH_3OH maser (Pestalozzi et al. 2006), as well as with the dominant cluster of H_2O masers (Kameya et al. 1990). Furthermore, it places NGC 7538 S on the symmetry axis of the compact bipolar outflow imaged in $\text{HCO}^+ J=1 \rightarrow 0$ and at the dynamical center of the rotating disk (Section 3.4.1).

3.3. Outflow and Accretion

We will discuss the molecular outflows in the NGC 7538 molecular cloud in more detail in (Corder et al, in preparation). In this section we re-examine the outflow, since it is intimately connected to the thermal jet and both must be powered by the accretion disk. The outflow parameters derived by Sandell, Wright & Forster (2003) are incorrect, because they were derived from $\text{HCO}^+ J=1 \rightarrow 0$ observations with the assumption that the outflow is cold and that the HCO^+ abundance is the same as in quiescent molecular cloud cores. However, Sandell, Goss & Wright (2005) analyzed the outflow from NGC 7538 IRS 9 and showed that the HCO^+ abundance

⁶ Recent sub-arcsecond continuum imaging at 110 and 224 GHz with CARMA (Paper II) resolve the elliptical core into three compact sources, all of which are almost certainly protostars. The strongest one of the three sources agrees within $0''.15$ with the adopted position for the high-mass protostar.

is enhanced by more than a factor of 30 compared to the “standard” OMC-1 ridge abundance. It is therefore clear that the HCO^+ abundances are likely to be enhanced in the NGC 7538 S outflow as well.

3.3.1. Outflow morphology

For NGC 7538 S we have many data sets that probe the outflow. Here we will largely restrict the discussion to $\text{CO } J=2\rightarrow 1$, $\text{CO } J=3\rightarrow 2$, $\text{HCO}^+ J=1\rightarrow 0$ and $\text{SiO } J=2\rightarrow 1$. CO is a very good outflow tracer and chemically much more robust than HCO^+ , although at near cloud velocities the emission can be optically thick. Figure 4 shows long integration spectra of $\text{CO } J=2\rightarrow 1$, $J=3\rightarrow 2$, and $^{13}\text{CO } J=2\rightarrow 1$, all obtained with JCMT. What we immediately see from these spectra is that the outflow is an extreme high-velocity outflow (Choi, Evans, & Jaffe 1993), because we see high-velocity wings extending to velocities $\geq 55 \text{ km s}^{-1}$ in both the blue- and the red-shifted side of the $\text{CO } J=2\rightarrow 1$ and $J=3\rightarrow 2$ spectra. The emission is strongly skewed to blue-shifted velocities, because of strong self-absorption. The self-absorption is even more extreme in $\text{HCO}^+ J=1\rightarrow 0$, where the red-shifted wing is almost completely absent (Figure 1) due to the strong accretion flow, see Section 3.3.3. The strong emission peak at -49 km s^{-1} , which dominates the emission on the red-shifted side of the CO lines, is due to the extended “ -49 km s^{-1} ” molecular cloud component, which is seen over most of the NGC7538 molecular cloud. The strong red-shifted self-absorption and the “ -49 km s^{-1} ” cloud make it difficult to derive accurate parameters for the red-shifted **lobe** and we will therefore restrict most of our discussion to the blue-shifted lobe.

Figure 5 shows the outflow imaged in HCO^+ . The outflow is clearly bipolar and very compact, suggesting that we are seeing a very young outflow. The position angle (p. a.) of the outflow determined from the HCO^+ high velocity emission is $\sim 148^\circ \pm 4^\circ$, i.e. roughly perpendicular to the position angle we derive for the accretion disk from $\text{H}^{13}\text{CN } J=1\rightarrow 0$ (Section 3.4.1). The position angle of the outflow agrees with the position angle of the thermal jet (Paper II, see also Figure 9), $145^\circ \pm 2^\circ$, which is to be expected if the outflow is powered by the jet. The blue-shifted lobe is extremely compact and extends only $\sim 8''$ to the NNW. The counter flow to the SSW contains both blue- and red-shifted high velocity gas, suggesting that the red-shifted lobe is somehow closer to the plane of the sky. The red-shifted lobe is more extended and less collimated. It looks more like a half shell without a clear front, suggesting that it has cleared the dense core and is expanding into a lower density regime. The extent of the red HCO^+ lobe is $\sim 16 - 17''$ and brighter on the western side. Examination of our $\text{CO } J=3\rightarrow 2$ map (Figure 6) shows a similar size in CO . The $\text{SiO } J=2\rightarrow 1$ outflow, however, appears more jet-like and extends to $\sim 22''$ from the central protostar (Figure 7).

HCO^+ and SiO show a red-shifted lobe of another outflow west of NGC 7538 S. It is also seen in our $\text{CO } J=3\rightarrow 2$ map, especially at high red-shifted velocities. It does not stand out very clearly in our single dish corrected HCO^+ image (Figure 5), which shows a strong broad red-shifted emission peak at $\sim 10''$ west of NGC 7538 S. Inspection of the HCO^+ data sets and the SiO image, however, suggests that it has a p.a. of $\sim 205^\circ$ and that it is brighter on the western side in HCO^+ . In Figure 5 this outflow is

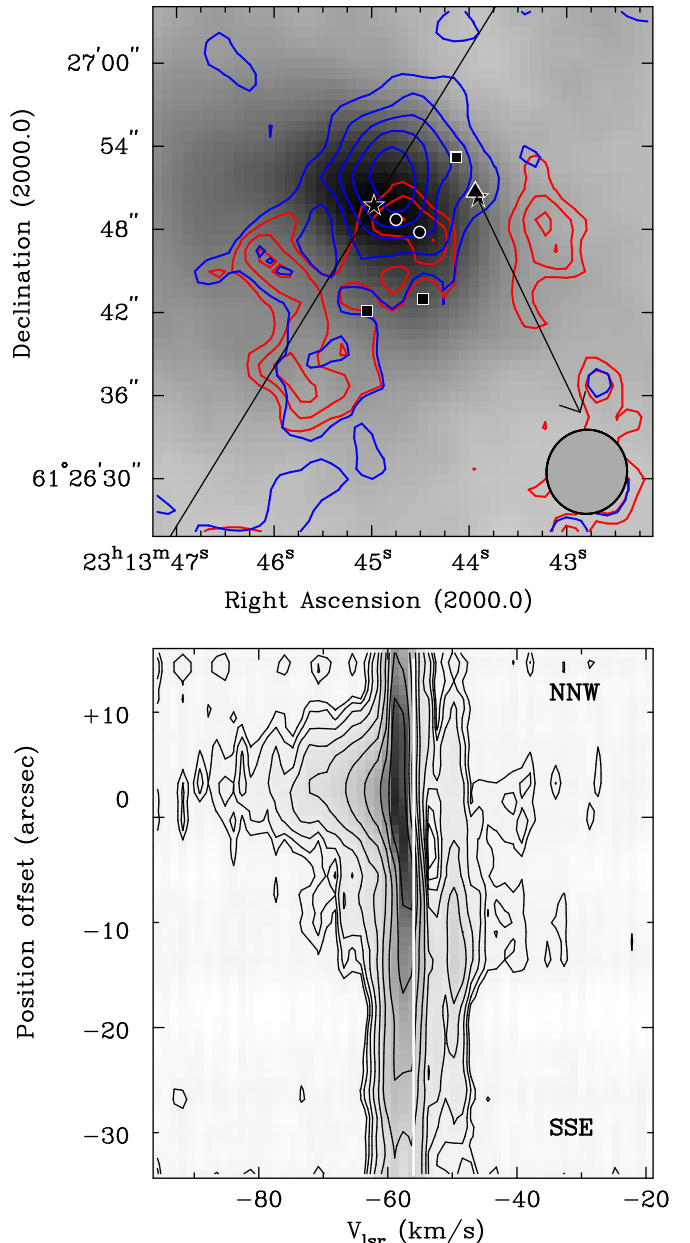


FIG. 5.— Top: Contour plot of the HCO^+ outflow overlaid on the integrated H^{13}CN emission (grey scale), which shows the distribution of the dense gas in the NGC 7538 S cloud core. The blue-shifted high velocity emission is integrated from -61 km s^{-1} to -80.7 km s^{-1} and plotted with blue contours. The contour levels are linear starting at 5 K km s^{-1} with a step size of 5 K km s^{-1} . The red-shifted high velocity emission is integrated from -49 km s^{-1} to -38.5 km s^{-1} and plotted with red contours. The contour levels are linear starting at 4 K km s^{-1} with a step size of 2 K km s^{-1} . The position of NGC 7538 S and IRS 11 S are marked by star symbols while the two new CARMA sources are marked with filled circles. The filled squares are Class I methanol masers and the triangle is an H_2O maser coinciding with IRS 11 S. The HPBW is indicated in the bottom right corner. The black line through NGC 7538 S shows the outflow axis at a position angle of 148° . The red-shifted peak at $12''$ west of NGC 7538 S is due to another outflow, possibly powered by IRS 11 S. It is also seen in SiO (Figure 7). Bottom: Position velocity plot as grey scale with contours along the outflow axis. The contour levels are logarithmic and plotted with 10 contours starting at 0.25 K to 14 K . The systemic velocity is marked by the white vertical line.

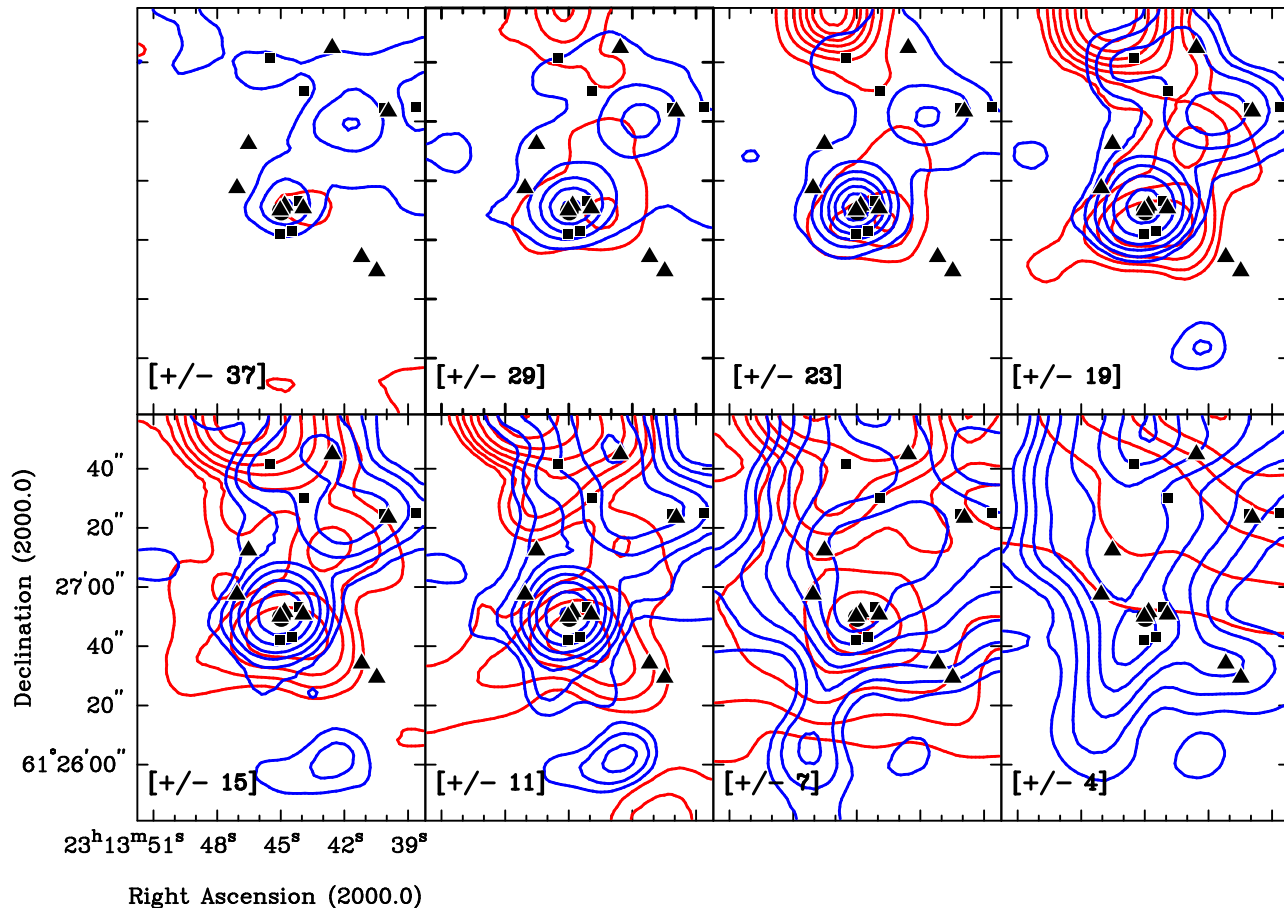


FIG. 6.— Maps of CO $J=3 \rightarrow 2$ high velocity emission integrated over eight different velocity intervals in blue- and red-shifted emission. The first velocity interval, bottom right panel, is 2 km s^{-1} centered at a velocity $\pm 4 \text{ km s}^{-1}$, the next five are integrated over 4 km s^{-1} wide velocity windows, and the last two over 8 km s^{-1} wide velocity intervals. The offset from the systemic velocity is indicated at the bottom right of each panel. The HPBW for these observations is $\sim 14''$, which is insufficient to resolve the outflow(s) from the NGC 7538 S core. At the very north we can see the strong red-shifted outflow from NGC 7538 IRS 1 (outside the area shown in these maps) and $\sim 40''$ northwest of NGC 7538 S, we see the blue-shifted lobe of another outflow. The contour levels start at 0.75 K km s^{-1} with a step of 7.5 K km s^{-1} . The filled triangles mark known H_2O masers, the squares CH_3OH Class I masers and the filled circle the position of NGC 7538 S.

shown with an arrow outlining the origin, extent ($\geq 17''$), and p.a. of the outflow. This red-shifted outflow has a rather high outflow velocity, $\sim 25 - 30 \text{ km s}^{-1}$, in both HCO^+ and SiO . It is almost certainly powered by the bright IRAC and H_2O maser source, IRS 11 S (Corder 2008, Paper II). There is no clear sign of a blue-shifted counter flow, although such a flow would overlap with the blue outflow lobe from NGC 7538 S.

3.3.2. Physical properties of the outflow

The high velocity emission is much stronger in CO $J=3 \rightarrow 2$ than in $J=2 \rightarrow 1$ (Figure 4), which indicates that the outflow is hot. Since the beam size is smaller for the CO $J=3 \rightarrow 2$ than the $J=2 \rightarrow 1$ transition, the higher intensities in CO $J=3 \rightarrow 2$ than in $J=2 \rightarrow 1$ are partly due to better coupling to the beam, but detailed analysis shows that the observed intensity ratios require the high velocity emission to have temperatures of 100 K or more. We do have maps of both CO $J=2 \rightarrow 1$ and CO $J=3 \rightarrow 2$ and we do know the size of the blue outflow lobe, enabling us to correct for beam filling. Nevertheless, it is difficult to derive an accurate temperature from only two CO transitions. We therefore prefer to use the ratio of the two formaldehyde transitions, H_2CO , $J=$

$3_{03} \rightarrow 2_{02}$ and $3_{22} \rightarrow 2_{21}$, which were observed simulta-

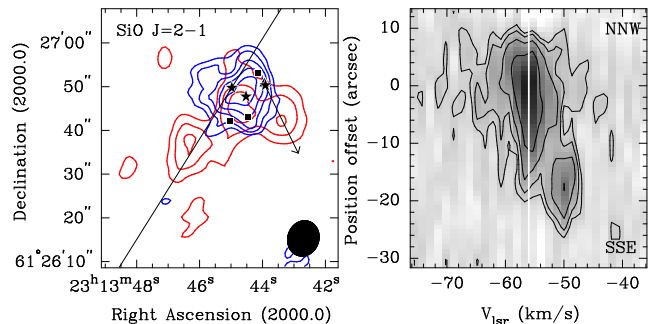


FIG. 7.— Left panel: Contour plot of the integrated $\text{SiO } J=2 \rightarrow 1$ high velocity emission. The blue-shifted high velocity emission is integrated from -61.4 km s^{-1} to -70.9 km s^{-1} and plotted with blue contours. The contour levels are linear starting at 1 K km s^{-1} with a step of 1 K km s^{-1} . The red-shifted high-velocity emission is integrated from -52 km s^{-1} to -39.8 km s^{-1} and plotted with red contours. The contour levels are linear starting at 2 K km s^{-1} with a step of 1 K km s^{-1} . The black line shows the position angle (148°) of the outflow, as determined from $\text{HCO}^+ J=1 \rightarrow 0$. Labeling is the same as in Figure 5. Right panel: Position velocity plot as grey scale with contours along the outflow axis. The contour levels are linear starting at 0.3 K with a step of 0.6 K . The systemic velocity is marked by the white vertical line.

neously with both BIMA and JCMT. These observations are therefore insensitive to calibration and pointing errors, and even though the line wings are much fainter in H_2CO than in CO we get a more accurate determination of the gas temperature in the outflow. The ratio $T_b(3_{03} - 2_{02})/T_b(3_{22} - 2_{21})$ is very sensitive to temperature, especially if the gas is not too hot (Mangum & Wootten 1993). If we integrate the blue-shifted wing from -59 km s^{-1} to -63 km s^{-1} , we find a ratio of 2.65 at the position of the protostar and ~ 2.9 in the blue outflow lobe. These line ratios correspond to kinetic temperatures of $\sim 120 \text{ K}$ at the position of the protostar and $\sim 100 \text{ K}$ in the outflow lobe (Mangum & Wootten 1993). For the red-shifted outflow lobe integrated over the velocity range -53 km s^{-1} to -50.5 km s^{-1} the ratios are 2.5 and 3.2, i.e. $140 \text{ K} - 80 \text{ K}$, at the position of the protostar and at the peak of the outflow lobe, respectively. The H_2CO data therefore confirm what we already saw from CO, i.e. the temperature of the gas in the outflow $\geq 100 \text{ K}$. A population diagram analysis of methylcyanide, $\text{CH}_3\text{CN } J=12 \rightarrow 11$, which also traces the high velocity gas (see Section 3.4.3), gives a rotational temperature of $147 \pm 40 \text{ K}$, in good agreement with what we derive from CO and H_2CO . Our H_2CO data suggest that the high velocity gas in the blue outflow is hotter near the surface of the disk and somewhat colder in the outflow lobe. The data also suggest that the blue-shifted gas could be somewhat hotter in the blue-shifted gas than the red-shifted gas, but this should be viewed with caution, since the red-shifted emission is affected by self-absorption from the infalling envelope.

Since the HCO^+ is often enhanced in outflows, it is not a good mass tracer (Sandell, Goss & Wright 2005). We therefore prefer to use ^{12}CO , which is more chemically robust. We have maps of the whole NGC 7538 S region in $^{12}\text{CO } J=2 \rightarrow 1$, i.e. the map published by Davis et al. (1998), $^{13}\text{CO } J=2 \rightarrow 1$, and in $^{12}\text{CO } J=3 \rightarrow 2$. We also have long integration spectra towards NGC 7538 S in $^{12}\text{CO } J=2 \rightarrow 1$, $^{13}\text{CO } J=2 \rightarrow 1$, and $^{12}\text{CO } J=3 \rightarrow 2$ (Figure 4). Even though the $^{12}\text{CO } J=3 \rightarrow 2$ goes deeper and has better spatial resolution than the $^{12}\text{CO } J=2 \rightarrow 1$ map, we will use the latter, because we have only a ^{13}CO map in $J=2 \rightarrow 1$, which allows us to estimate the optical depth in the outflow. The long integration ^{13}CO spectrum shows high velocity wings over the velocity range -70 km s^{-1} (possible even -80 km s^{-1}) to -38 km s^{-1} , confirming that most of ^{12}CO emission is optically thick. The main disadvantage of using single dish ^{12}CO data, is that the CO emission is very strong and extended over a large velocity range, from about -65 km s^{-1} to -48 km s^{-1} , even though the blue outflow lobe can be seen in channel maps at lower velocities (Figure 6). In order to capture the low velocity gas we have therefore subtracted out the extended background emission from the compact outflow emission. The background emission was estimated in several areas and normalized to the same area we integrated over in the map. For analysis of the long integration spectra, we average spectra in the same background regions and integrated the background spectrum over the same velocity range. Since the $^{12}\text{CO } J=2 \rightarrow 1$ map has relatively poor signal-to-noise, we found that we get more accurate mass estimates by using the long integration CO spectra rather than integrating over

the map, since the outflow is very compact and we know the size very well from our BIMA imaging in HCO^+ . Furthermore, using long-integration CO spectra allows us to trace the outflow to much higher velocities, which is important for estimating the energy of the outflow. Because we had to create reference spectra in both ^{12}CO and ^{13}CO from positions outside the outflow, the biggest uncertainty in our mass estimate is due to the opacity correction at low velocities, which depends on how well we subtracted out the extended cloud emission. If we assume that the bulk of the gas has a temperature of 100 K , and a $[\text{CO}/\text{H}_2] = 10^{-4}$, our $^{12}\text{CO } J=2 \rightarrow 1$ data give an outflow mass of $6.5 M_\odot$, over the velocity range -60 km s^{-1} to -111 km s^{-1} . About 75% of this mass resides at low outflow velocities, $<10 \text{ km s}^{-1}$. The momentum of the blue outflow lobe, $P_{blue} \sim 50 M_\odot \text{ km s}^{-1}$, and since it is natural to assume that the momentum is conserved, we get $P \sim 100 M_\odot \text{ km s}^{-1}$ for the whole outflow. These values are not corrected for the inclination of the outflow. We should note, however, that the blue outflow lobe most likely also includes the outflow from other sources in NGC 7538 S (see paper II), and perhaps even the IRS 11 S outflow, see Section 3.3.1.

Since we now have mass estimates of the outflow from CO, we can determine how much the HCO^+ abundance is enhanced in the outflow using our combined BIMA and FCRAO outflow map. If we assume normal HCO^+ abundances, i.e. $[\text{HCO}^+/\text{H}_2] = 2.8 \cdot 10^{-9}$, and optically thin HCO^+ emission (Hogerheijde et al. 1998), we get an outflow mass of $31.6 M_\odot$, suggesting that HCO^+ is enhanced by about a factor of five. This enhancement is more modest than in the IRS 9 outflow, where Sandell, Goss & Wright (2005) found HCO^+ enhanced by a factor of 30. However, if we only compare the mass estimates at high velocities, we find that the HCO^+ abundance is enhanced by a factor of 20 - 40, suggesting that enhancement of HCO^+ is caused by shocks from the high velocity outflow.

In order to determine the mass loss rate and energetics of the outflow, we need to know the age of the outflow. The age is typically determined from the dynamical time scale, corrected for the inclination of the outflow (Cabrit & Bertout 1990). It is difficult to accurately estimate the inclination of the outflow. However, since we have a wide-angled outflow and there is some overlap between the blue and the red-shifted outflow lobe, a comparison of the different model cases computed by Cabrit & Bertout (1990), suggests an inclination angle between $40^\circ - 60^\circ$. In the following we assume an inclination angle of 50° . If we take the mass weighted outflow velocity for the blue outflow lobe, which is $\langle V \rangle = 7.3 \text{ km s}^{-1}$, we get dynamical time scale, $t_d = 12,200 \text{ yr}$. This is likely to be an under-estimate, since it does not account for the time it has taken the outflow to expand into the massive, dense cloud core surrounding the outflow. We will therefore also examine the red outflow lobe. Here we cannot derive a reliable mass estimate, because the red-shifted gas velocity is heavily self-absorbed, especially at low velocities. We therefore use the terminal velocity at the tip of the flow, $\sim 0.3 \text{ pc}$ from the star ($22''$), which is 17 km s^{-1} for $\text{HCO}^+ J=1 \rightarrow 0$. In this case we get a dynamical time, $t_d = 14,000 \text{ yr}$, about the same as we derived for the blue outflow lobe. It is probably an under-

estimate, because the mass-weighted velocity is likely to be lower than the terminal velocity that we used. We can get a third estimate of the outflow rate from theoretical models of collapsing cloud cores, which suggest that outflows form at about 0.6 times the free-fall time, τ_{ff} (Tomisaka 1998). The average gas density in the elliptical core surrounding NGC 7538 S is $\sim 10^7 \text{ cm}^{-3}$, resulting in $\tau_{ff} = 2.5 \cdot 10^4 \text{ yr}$, which would suggest that the outflow started about 15,000 yrs ago, in reasonable agreement with what we deduced from the dynamical time scales. If we assume an outflow age of 15,000 yr, we find a mass loss rate of $\sim 4.3 \cdot 10^{-4} M_{\odot} \text{ yr}^{-1}$, if the red outflow lobe has a similar mass as the blue lobe. With these assumptions we derive a momentum flux, $F = 1.0 \cdot 10^{-2} M_{\odot} \text{ km s}^{-1} \text{ yr}^{-1}$, a mechanical luminosity of $14.2 L_{\odot}$, and a kinetic energy of $1.3 \cdot 10^3 M_{\odot} (\text{km s}^{-1})^2$ or $2.6 \cdot 10^{46}$ ergs. The derived momentum flux would suggest that the exciting star or stars have a bolometric luminosity of $10^4 L_{\odot}$, if we use the correlation by Beuther et al. (2002a) derived for Class I and young high-mass objects, which is close to the observed luminosity. For Class 0 objects Bontemps et al. found an outflow efficiency ~ 10 higher than for Class I objects, but this is not true for NGC 7538 S, even though in any other respect it appears to be a Class 0 object. It is possible that this relationship does not hold for extremely young outflows, which are still density bounded.

3.3.3. Accretion flow

The red-shifted outflow wing is almost completely absent in $\text{HCO}^+ J=1 \rightarrow 0$ (Figure 1), suggesting that it is self-absorbed by the cold, infalling cloud envelope. We know that NGC 7538 S is surrounded by a dense, cold ($\sim 25 \text{ K}$) massive envelope ($\sim 2,000 M_{\odot}$), where most molecules (including HCO^+) are optically thick (Section 3.1). If the cloud core was in thermal equilibrium, one would therefore expect to see a symmetric line profile around the systemic velocity of the cloud core, but the absorption appears to affect only the red-shifted velocities. Our long integration CO spectra, Figure 4, see Section 3.3.1, show that the outflow velocities are the same in the blue- and the red-shifted wing. Therefore the absence of red-shifted HCO^+ emission is not because the red-shifted emission is absent, but because it is self-absorbed by the outflow. This is confirmed by our observations of $\text{SiO } J=2 \rightarrow 1$, and $\text{SO } J=5_5 \rightarrow 4_4$, which both show symmetric high velocity wings over the velocity interval, where emission from HCO^+ is very weak or absent. Since the SiO and SO transitions come from much higher energy levels, the absence of self-absorption in these lines suggest that they are not sufficiently excited in the cold surrounding cloud envelope to cause self-absorption against the hot outflow. The red-shifted self-absorption, which is so striking in HCO^+ must therefore be caused by infall of the cloud core surrounding NGC 7538 S. To illustrate this more clearly, we have taken the $\text{SO } J=5_5 \rightarrow 4_4$ line, which was observed with a similar beam size as HCO^+ and scaled it, so that it roughly matches the HCO^+ profile (Figure 8). From this figure we can see that infall starts to affect the red-shifted outflow from velocities $\sim -40 \text{ km s}^{-1}$. We can directly create an infall profile by fitting two Gaussians (one for the cloud core and one for the outflow) to the

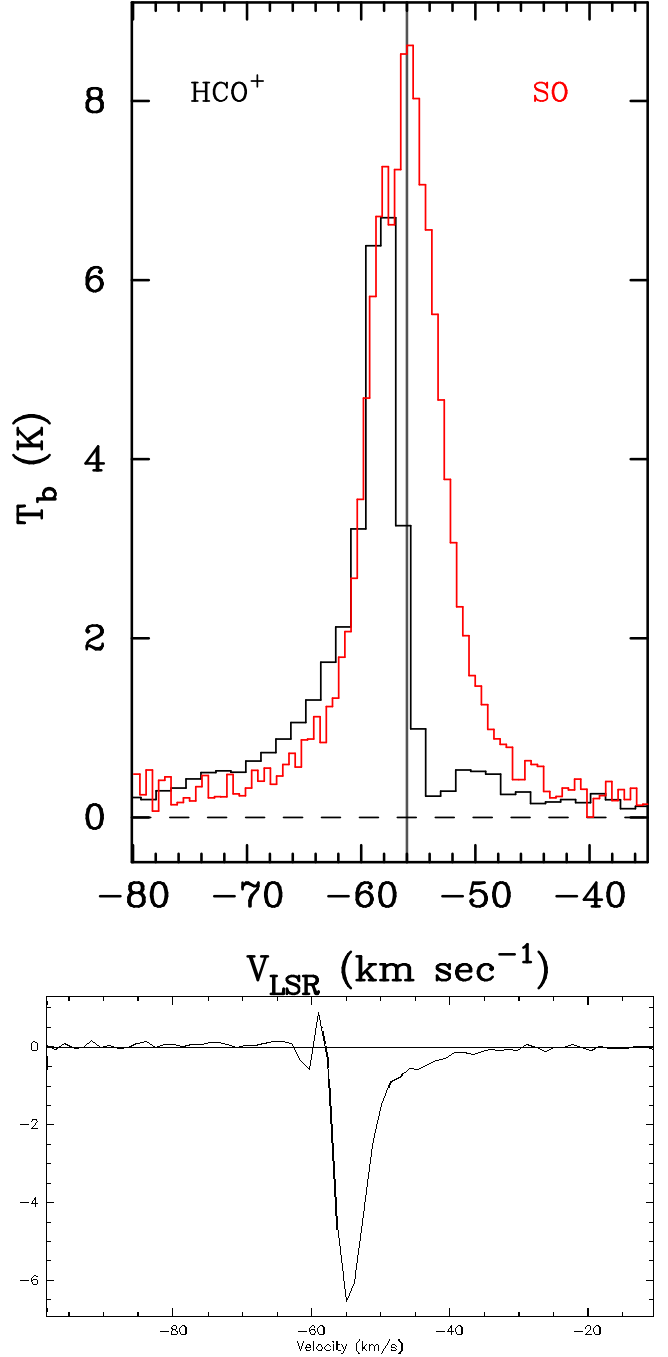


FIG. 8.— The top panel shows the $\text{HCO}^+ J=1 \rightarrow 0$ spectrum towards NGC 7538 S. Overlaid on the HCO^+ profile, we have plotted the $\text{SO } J=5_5 \rightarrow 4_4$ line at the same position in red, which has been scaled to match HCO^+ spectrum. This SO transition is not affected by self-absorption and shows symmetric blue- and red-shifted wings from the outflow. In the bottom panel we show the residual of a two component Gaussian fit to the blue side of the HCO^+ spectrum. This residual represents the predicted absorption profile of cold optically thick gas in front of the hot NGC 7538 S outflow assuming that in absence of absorption, the HCO^+ profile would be similar to SO , i.e. have symmetric blue- and red-shifted wings. The absorption profile is dominantly red and extends to $\sim -40 \text{ km s}^{-1}$.

blue-shifted side of the HCO^+ profile and blanking out the part of the spectrum which is likely to be affected by self-absorption. If we subtract the fit from the observed spectrum, we get the absorption profile shown in Figure 8, which confirms that we can see the infall to at least 16 km s^{-1} . At the systemic velocity, HCO^+ is optically thick. The ratio of the the peak intensity of HCO^+ to H^{13}CO^+ (Table 3, Figure 8) is ~ 2 , if we use the fitted peak for HCO^+ , 6.5 K , and ignore any differences in beam size. This corresponds to an optical depth of ~ 20 (for a $^{12}\text{C}/^{13}\text{C}$ abundance of 40). At the peak of the absorption profile we therefore have an optical depth of 10. Inspection of position velocity plots (Figure 5) and spectra around NGC 7538 S indicates that we see narrow self-absorption out to a radius of at least $15''$ while the self-absorption at high velocities is only seen in the immediate vicinity of NGC 7538 S, indicating that the accretion flow is accelerating. In order to estimate the mass of the infalling cloud envelope, we somewhat arbitrarily divide the absorption profile into two parts: an extended low velocity component ($V > -54 \text{ km s}^{-1}$) with a FWHM of $\sim 6''$, and an unresolved component extending to velocities $\sim -40 \text{ km s}^{-1}$. The low velocity infall component has an integrated intensity of $\sim 14 \text{ K km s}^{-1}$ and an assumed average optical depth of ~ 3 , while the integrated intensity of the unresolved “high velocity” infall is 23.5 K km s^{-1} . Since we see the gas in absorption, it must have an optical depth about one or more. If we sum up the gas seen in absorption, we get $\sim 125 \text{ K km s}^{-1}$, which is half the infalling gas, since we have an equal amount from the backside of the cloud. If we adopt an $[\text{HCO}^+/\text{H}_2]$ abundance of $2.8 \cdot 10^{-9}$ and a kinetic temperature of 25 K , we get a mass of $21 M_\odot$, which is strictly speaking a lower limit. If we assume that the time scale for accretion is the same as for the outflow, i.e. $15,000 \text{ yr}$, we get a mass accretion rate $\sim 1.4 \cdot 10^{-3} M_\odot \text{ yr}^{-1}$.

A more common way to estimate the accretion rate is to assume that the outflow rate is proportional to the accretion rate, see e.g. Beuther et al. (2002a). If we assume that the ratio of the outflow rate and the accretion rate is approximately 0.3 (Tomisaka 1998; Shu et al. 1999) we get an accretion rate of $1.4 \cdot 10^{-3} M_\odot \text{ yr}^{-1}$, the same as what we got from our direct estimate of the infalling cloud mass. The agreement is probably fortuitous, because both estimates have an uncertainty of at least a factor of two or three.

Another way to estimate the accretion rate is to assume that we have a steady state accretion flow with an infall velocity, v_{infall} , onto a uniform disk with a radius, R , and a surface density, Σ , see e.g. Beltrán et al. (2004). In this case the mass accretion rate, \dot{M}_{acc} , can be expressed as: $\dot{M}_{\text{acc}} = 2\pi R v_{\text{infall}} \Sigma$. Allen et al. (2003), who did numerical simulations of the collapse of a magnetized molecular cloud core assumed to undergo rigid rotation, show that in such a case the infall velocity is the same as the rotation velocity of the disk. Since we measure a rotational velocity of $\sim 1.3 \text{ km s}^{-1}$ at a radius of $\sim 7000 \text{ AU}$ (Section 4.1) and with a surface density, $\Sigma = 2.1 \text{ g cm}^{-2}$, deduced from our H^{13}CN observations of the disk (Section 3.4), we find an accretion rate, $\dot{M}_{\text{acc}} = 2.8 \cdot 10^{-3} M_\odot \text{ yr}^{-1}$, twice as large than our two other estimates, but well within the errors of each method.

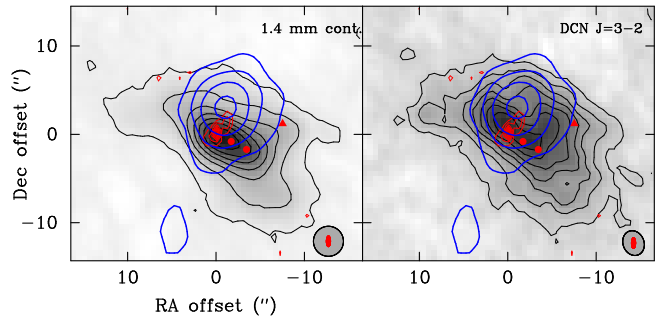


FIG. 9.— Gray scale images of total integrated DCN $J=3 \rightarrow 2$ emission (right panel) and 1.4 mm continuum emission (left panel) overlaid with black contours. Overlays: 3.6 cm continuum emission (red contours), and HCO^+ blue shifted emission (blue contours). The red triangle marks the H_2O maser associated with the mid-IR source IRS 11 S and the filled circles the two new CARMA sources discovered in the elliptical core.

3.4. The compact core and the accretion disk

Both DCN $J=3 \rightarrow 2$ and $\text{H}^{13}\text{CN } J=1 \rightarrow 0$ show an elliptical source approximately centered on NGC 7538 S superposed on more extended fainter emission. In the left panel of Figure 9 we show the integrated DCN emission, overlaid with the 3.6 cm continuum emission from Paper II, and the blue-shifted HCO^+ emission, which show how the jet and the outflow relate to the disk-like structure seen in the integrated DCN image. In the right panel of Figure 9 we show the 1.4 mm continuum emission (Paper II), also overlaid with the blue-shifted HCO^+ emission. The dust continuum and the DCN emission look very similar, although there appears to be more structure in the DCN emission than in the dust continuum emission, even though both have been imaged with very similar spatial resolution. The integrated DCN emission shows a ridge-like structure extending to the northwest $\sim 4''.5$ west of NGC 7538 S. This ridge or DCN “clump” is not seen in the dust continuum, but it does show up in H^{13}CN , but only at high spatial resolution (Figure 10, right panel). As we can see from Figure 9 this DCN condensation borders the western side of the blue outflow, and could therefore be a dense gas clump compressed by the outflow (Section 3.4.2). A few arcseconds west of the DCN clump is another IRAC (mid-infrared) source, IRS 11 S, but the DCN clump is rather compact ($\sim 3''$) and the positional offset is too large to suggest an association with this source. IRS 11 S is clearly another young star, because it excites an H_2O maser and powers a small outflow.

Gaussian fits to the dust continuum and to the integrated H^{13}CN emission give a size for the compact core of $\sim 10'' \times 4''$ at p.a. $58^\circ \pm 3^\circ$, centered $\sim 2''$ southwest of the center of the accretion disk. If we assume a gas temperature of 35 K , and an $[\text{H}^{13}\text{CN}/\text{H}_2]$ abundance of 1.25×10^{-10} , i.e. the same abundance that we assumed for the NGC 7538 S cloud core, see Section 3.1, we obtain a total mass of $85 M_\odot$. This mass estimate is very similar to what we derive from our dust continuum observations, $\sim 125 M_\odot$ (Paper II). Even though we do not have a good estimate for the gas temperature in the compact core, our assumed temperature appears reasonable. The lowest measured gas temperature comes from ammonia, 25 K . This gives a lower limit to the gas temperature. The temperature of the disk is certainly < 50

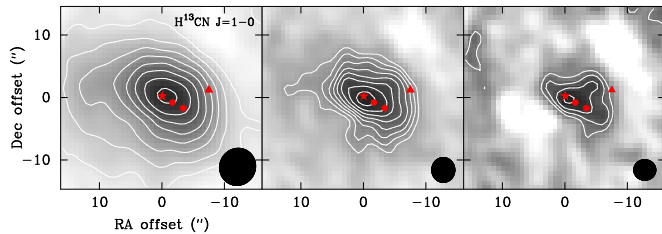


FIG. 10.— Grayscale images of Integrated H^{13}CN $J=1\rightarrow 0$ emission overlaid with contours for three different angular resolutions. The image to the left is created from all data sets using natural weighting, while the one in the middle has been made with robust weighting and excluding all uv-spacings shorter than $5\text{ k}\lambda$. The image to the right, which has the highest angular resolution, was made with natural weighting and excluding all uv-spacings shorter than $10\text{ k}\lambda$, shows the disk most clearly, but has rather poor signal-to-noise. The symbols are the same as in Fig. 9, except for NGC 7538 S, which is now marked with a red star symbol.

K (see Section 3.4.3). Since the gas mass scales roughly linearly with temperature, the largest error in our gas mass estimate is due to the uncertainty of the H^{13}CN abundance.

Of all the molecules that we have observed in the 3 mm band, it appears that the best molecular tracer of the disk is H^{13}CN $J=1\rightarrow 0$. As far as we can tell, the H^{13}CN emission is only weakly contaminated by the high-velocity outflow, and we have sensitive maps obtained with relatively high spatial resolution ($\sim 3''9$). We also observe a clear velocity gradient along the major axis of the disk in HN^{13}C $J=1\rightarrow 0$ and H^{13}CO^+ $J=1\rightarrow 0$ in the same direction as in H^{13}CN , i.e. blue-shifted emission to the northeast and red-shifted emission to the southwest. A position-velocity cut of H^{13}CO^+ along the outflow direction shows blue-shifted emission to the northwest and red-shifted emission to the southeast, i.e. H^{13}CO^+ is clearly affected by the outflow, which makes it very difficult with this angular resolution to dis-entangle how much of the observed velocity gradient comes from the disk and how much of it is due to the outflow. For these lines we have only one B- and one C-array track giving us an angular resolution of $\sim 7''8$ (Table 1). Since the data are rather noisy and have poorer spatial resolution than H^{13}CN , we will not discuss them further in this paper.

At 1.4 mm we have high signal-to-noise maps in DCN $J=3\rightarrow 2$ and CH_3CN $J=12\rightarrow 11$, with even higher spatial resolution ($\sim 2''6$) than H^{13}CN $J=1\rightarrow 0$. However, although DCN $J=3\rightarrow 2$ appears to trace the accretion disk, the emission is rather strongly affected by emission from the outflow, making it difficult to accurately determine the rotation curve for the disk, although the values we derive are in reasonable agreement with what we find from H^{13}CN (Section 3.4.1). Although Cesaroni et al. (1999, 2005) find CH_3CN to be a good disk tracer for the young high-mass star IRAS 20126 + 4104, we find that CH_3CN is dominated by emission from the outflow, which effectively masks any emission from the underlying accretion disk (Section 3.4.3).

Below we discuss in detail the findings for these three molecules.

3.4.1. H^{13}CN $J=1\rightarrow 0$

Emission from H^{13}CN $J = 1 \rightarrow 0$ is widespread over the whole NGC 7538 molecular cloud, with the strongest emission in the whole cloud being centered on NGC 7538 S. Here we are interested only in emission from

TABLE 4
RADIAL VELOCITIES AND LINE-WIDTHS OF
 H^{13}CN $J=1\rightarrow 0$ IN THE ACCRETION DISK

Position ^a	V_{LSR} [km s^{-1}]	ΔV [km s^{-1}]
HPBW = 6.0×5.7		
northeast	-56.59 ± 0.06	3.9 ± 0.1
center	-55.98 ± 0.07	4.7 ± 0.1
southwest	-55.19 ± 0.16	4.6 ± 0.4^b
HPBW = 4.0×3.7		
northeast	-57.34 ± 0.11	3.1 ± 0.3
center	-55.97 ± 0.12	5.5 ± 0.1
southwest	-54.17 ± 0.59	4.4 ± 0.6^b
HPBW = 3.5×3.3		
northeast	-57.76 ± 0.21	2.3 ± 1.0
center ^c
southwest	-54.33 ± 0.89	5.5 ± 0.8^b

^a Positions southwest and northeast are at $\pm 2''5$ from the center at a p.a. of 58° .

^b At the southwest position the red-shifted emission from the disk is blended by emission from the surrounding cloud core, resulting in uncertain velocities and broadened line widths.

^c The line is too deeply self-absorbed to result in a successful fit.

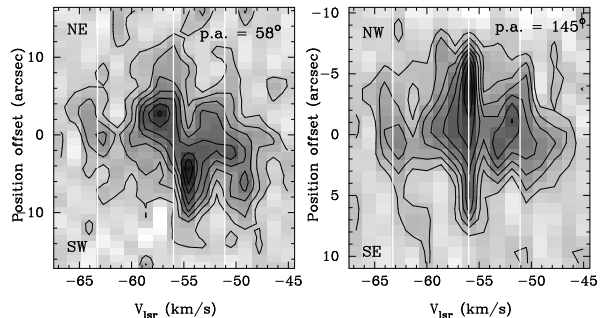


FIG. 11.— Position velocity cuts of H^{13}CN $J=1\rightarrow 0$ emission along the disk plane (left panel) and along the outflow (right panel). The vertical white lines mark the 3 hyperfine components at the systemic velocity.

the disk, and we would prefer to completely filter out all the extended emission surrounding the accretion disk. We have therefore created several images, where we have excluded short spacings, and we have also experimented with weighting the uv-data in different ways. However, since most of our data come from relatively short spacings, this has a severe penalty in signal-to noise. Figure 10 shows the integrated H^{13}CN emission with three different angular resolutions. We will base most of our analysis on the central image, which was created by excluding all uv-spacings shorter than $5\text{ k}\lambda$ and using robust weighting, giving an angular resolution of $4''0 \times 3''7$, p.a. = 0.2° , and still resulting in a good signal-to-noise ratio. Figure 11 shows position velocity plots along the disk-plane (p.a. = 58°) and in the outflow direction (p.a. = 145°). The H^{13}CN emission shows a very distinct velocity gradient over the disk, with blue-shifted emission to the northeast and red-shifted emission to the southwest. At the center of the accretion disk the main hyperfine

component ($F = 2 \rightarrow 1$) appears to be self-absorbed. The self-absorption is hardly visible in spectra at lower angular resolution, i.e. our naturally weighted map (Figure 1), while the line is almost completely absent at our highest angular resolution. The highest blue- and red-shifted emission peaks $\sim \pm 2''.5$ from the center of the disk, suggest a diameter of $\sim 5''$ or $\sim 14,000$ A.U. for the rotating disk. DCN $J=3 \rightarrow 2$ gives similar results for the disk size (Section 3.4.2).

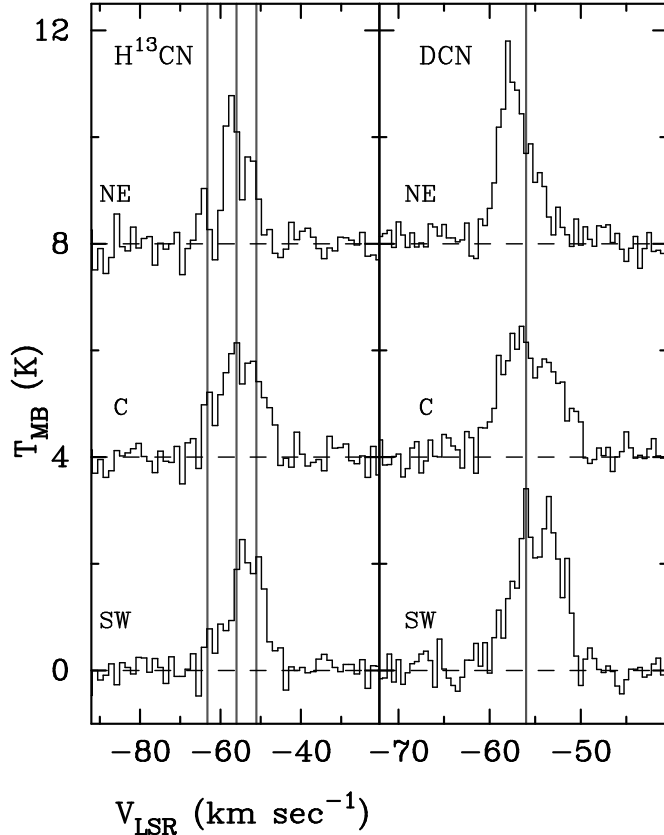


FIG. 12.— Spectra from the blue-shifted edge (NE, offset $2''.12, +1''.32$), center ($0'', 0''$), and red-shifted edge (SW, offset $-2''.12, -1''.32$) of the disk for the high angular resolution, robust weighted $H^{13}CN$ $J=2 \rightarrow 1$ image (left panel) and for DCN $J=3 \rightarrow 2$ (right panel). For both molecules we have indicated the systemic velocity and for $H^{13}CN$ additionally the velocities of the two hyperfine lines relative to the main line, $F = 2 \rightarrow 1$.

We made Gaussian fits of spectra extracted from all three images in order to more precisely quantify the velocity gradient. These Gaussian fits were made using method `hfs` in CLASS, which results in very reliable velocity information, since it uses the information from all three hyperfine lines. We also made Gaussian fits by locking the hyperfine lines to the main line, but since the lines are blended this requires us to keep the line width constant in order to get reliable fits. The two methods give similar results to within ± 0.1 km s^{-1} . In Table 4 we give the results obtained with method `hfs`. We can see from this table that higher spatial resolution results in larger velocity shifts at the edge of the disk and narrower line widths, as one would expect, because we get less velocity smearing within the beam. At the western side of the disk the emission from the surrounding cloud core is

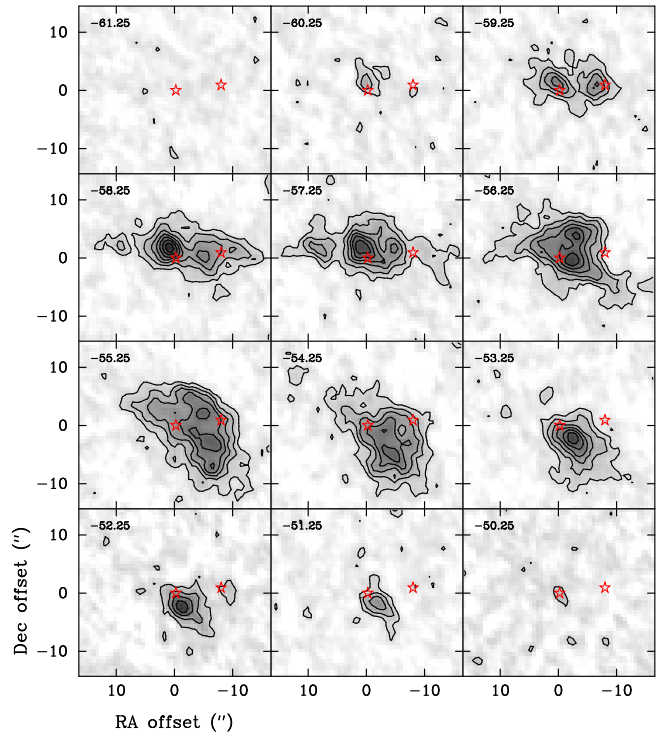


FIG. 13.— DCN $J=3 \rightarrow 2$ channel maps in grayscale overlaid with contours. Each panel shows the DCN emission integrated over a 1 km s^{-1} wide velocity interval. The center velocity of each map is indicated at the top left of each panel. The two star symbols mark the position of NGC 7538 S (at $0'', 0''$) and IRS 11 S. The contours are linear starting at 0.12 Jy beam^{-1} with a step size of 0.12 Jy beam^{-1} .

blended with the emission from the disk. This is seen better in DCN $J=3 \rightarrow 2$, which has negligible hyperfine splitting, see Figure 12.

As we can see from the position velocity plot along the outflow (Figure 11), even $H^{13}CN$ shows some emission from the outflow, because the emission northwest of the disk is blue-shifted, while there may be some red-shifted emission to the southeast.

3.4.2. DCN $J=3 \rightarrow 2$

The emission from DCN $J=3 \rightarrow 2$ is more compact than $H^{13}CN$ $J=1 \rightarrow 0$ and also appears more lumpy than the $H^{13}CN$ emission, c.f. Figures 9 & 10. To some extent this is to be expected, since the spatial resolution is much higher in DCN than in $H^{13}CN$ (Tables 1 & 2). At the highest angular resolution, $\sim 3''.5$, that we could achieve from our $H^{13}CN$ observations (Figure 10, right panel), $H^{13}CN$ does appear to show a second condensation $\sim 4''.5$ west of NGC 7538 S, which is also seen in DCN. However, the difference in morphology between the DCN emission and $H^{13}CN$ emission is too large to be a result from angular resolution alone. To get a better idea where the DCN emission comes from, we created a set of images with 1 km s^{-1} spacing over the whole velocity range where we see DCN emission. These channel maps are shown in Figure 13. At the highest red- and blue-shifted velocities, the emission peaks on or near the center of NGC 7538 S, while at near cloud velocities the emission is stronger to the NE or the SW of the protostar, depending on whether we look at blue-shifted or red-shifted emission. At slightly blue-shifted velocities (~ -58 km s^{-1}) DCN

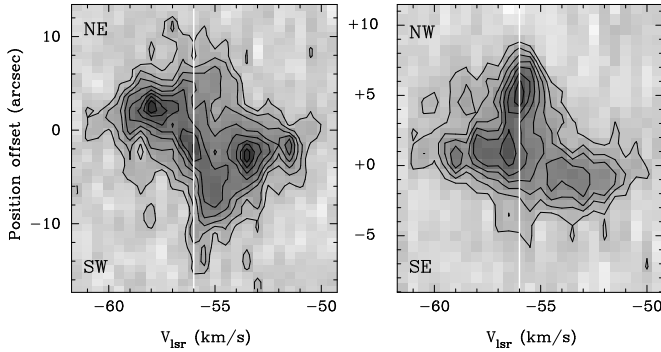


FIG. 14.— Position velocity plots of DCN $J=3\rightarrow 2$ emission in grayscale overlaid with contours. The contours are linear starting at $0.15 \text{ Jy beam}^{-1}$ and a step size of $0.10 \text{ Jy beam}^{-1}$. The left panel shows a cut along the disk plane (p.a. = 58°), while the right panel shows a cut along the outflow (p.a. = 145°). The systemic velocity is indicated with a vertical line. The direction of the cuts is indicated at top and bottom left of each figure. NGC 7538 S is at offset 0.

shows an E-W ridge with three dominant peaks. The strongest one is slightly north northwest, $\sim 1 - 2''$, of NGC 7538 S, with another fainter core at $+9'', +2''$ relative to NGC 7538 S. To the west there is another peak at $-5'', +1''$ and an even fainter one at $-10'', +1''$. None of the DCN peaks, except the central one, coincide with any known object in the NGC 7538 S cloud core. The H_2O maser and IRAC source, IRS 11 S, the other known young active object in the vicinity of NGC 7538 S, is roughly halfway between the two western cores. At the cloud velocity the strongest emission is $\sim -2''$ west of S, but here we see another very strong peak at $-3'', +4''$. The line at this position is centered at the cloud velocity (-56 km s^{-1}), and has a very narrow line width, $\sim 1 \text{ km s}^{-1}$, with a faint blue-shifted shoulder. At red-shifted velocities most of the DCN emission comes from an extended ($\sim 10''$) region southwest of NGC 7538 S. Although each velocity interval shows several red-shifted DCN clumps, the position of these clumps move when going from one velocity to the next, suggesting velocity gradients or turbulent gas. This is also seen in spectra from the southwestern part of the core, which are much broader with line widths of $4 - 5 \text{ km s}^{-1}$.

If we integrate over 5.5 km s^{-1} centered on $V_{lsr} = -56 \text{ km s}^{-1}$, i.e. roughly the velocity spread that we see in H^{13}CN , we see a central “disk-like” feature, similar to what we see in H^{13}CN , but with a northwestern ridge curving up from the southwestern edge of the “disk”, i.e. very similar to the integrated DCN emission shown in Figure 9. However, the channel maps show that this is not really a ridge, but a blending of the DCN clump at $-5'', +1''$. The double-peaked “disk”, however, is centered about somewhat west ($\sim 1''$) of the protostar. Even though this “disk” has roughly the same position angle as the continuum and H^{13}CN disk, it is also shifted about one arcsecond to the north, making it questionable whether it is really a disk.

We have therefore made position velocity plots centered on the protostar along the disk plane and in the outflow direction (Fig 14), i.e. the same cuts as we did for H^{13}CN . These position velocity plots clearly demonstrate that DCN is strongly affected by the outflow. The total velocity extent of the DCN emission is $\sim 11 \text{ km s}^{-1}$, which is far more than we would expect to see from a ro-

tating Keplerian disk. Furthermore, the cut along the outflow shows that the blue-shifted emission is to the north-west and the red-shifted emission is to the south-east of NGC 7538 S. The “high-velocity” DCN outflow is much more compact, only a few arcseconds, than the outflow we see in HCO^+ , which extends $\sim 8''$ to the northwest and even further in the red-shifted outflow lobe. However, at low blue-shifted velocities, DCN has a similar extent as HCO^+ . In the cut along the disk, there is a clear blue-shifted velocity gradient to the northeast, and red-shifted to the southwest. The red-shifted emission to the southwest of the disk center is partly suppressed by red-shifted self-absorption, see Figure 1 and Table 3, which quenches the emission on the red-side. There is apparently a velocity component at $\sim -55 \text{ km s}^{-1}$ extending $\sim 10''$ to the southwest, which gives the appearance of a velocity gradient across the disk. However, the velocity feature we would associate with the disk, is the strongest red-shifted peak $\sim 2''.6$ to the southwest at a velocity of -53.5 km s^{-1} . The corresponding blue-shifted peak is at $2''.5$ to the northeast at a velocity of -58.0 km s^{-1} . There is, however another fainter even more red-shifted ($V_{lsr} \sim -51.5 \text{ km s}^{-1}$) peak $\sim 2''$ to the southwest, which is probably from the outflow.

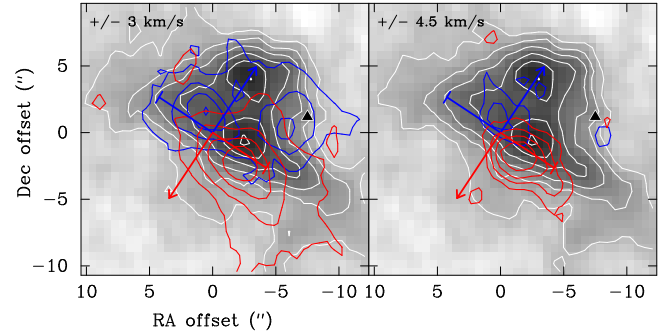


FIG. 15.— Grayscale image of DCN $J=3\rightarrow 2$ emission overlaid with white contours and integrated over 1.5 km s^{-1} (3 channels) centered on the cloud velocity, -56 km s^{-1} . The grayscale image is overlaid with blue- and red-shifted emission plotted with thick blue and red contours. In the right panel we show emission integrated over 1.5 km s^{-1} and shifted by 3 km s^{-1} relative to the cloud velocity, while the emission in the right panel is shifted by 4.5 km s^{-1} . The plane of the disk is indicated by a line going through the center at a p.a. of 58° and colored blue and red on the blue- and red-shifted side of the disk, respectively. The position, extent, and direction of the outflow is indicated with arrows, blue to the northwest and red to the southeast.

To get a better idea of where the blue- and red-shifted emission comes from, we overlaid the blue- and red-shifted DCN emission in two different velocity intervals on the integrated DCN emission of the cloud core (Figure 15). At a velocity offset of $\pm 3 \text{ km s}^{-1}$ most of the blue-shifted emission is to the north northwest, i.e. what one would expect if the emission comes from the disk surface and/or the shearing layer between the outflow and the surrounding cloud. There is also a clear north-east southwest gradient, although with a somewhat different position angle, p.a. $\sim 40^\circ$, than what we deduced from H^{13}CN . At higher velocities, $\pm 4.5 \text{ km s}^{-1}$ the blue- and red-shifted DCN emission moves more in the outflow direction, suggesting that most of the emission originates from the outflow. In both velocity intervals, however,

we see very little red-shifted emission to the east. This could suggest that some of the red-shifted emission is neither associated with the disk nor the outflow from NGC 7538 S, but instead comes from more red-shifted gas clumps in the cloud core.

Since DCN $J=3 \rightarrow 2$ is strongly affected by the outflow, it is not an ideal disk tracer. If the dominant velocity peaks seen in the position velocity plot along the disk plane at $\sim \pm 2''.5$ originate from a rotating disk, the DCN emission would suggest a systemic velocity of -55.8 km s^{-1} , a velocity shift of 4.5 km s^{-1} for a disk size of $5''.1$, i.e. very similar in size to what we get from H^{13}CN , but with a larger velocity difference. We can also see this in Figure 12, where we show spectra of both H^{13}CN and DCN in three positions of what we interpret as the rotating accretion disk surrounding NGC 7538 S. Both molecules are blue-shifted to the northeast, both show some evidence for slightly red-shifted narrow self-absorption towards the center of the disk and red-shifted emission to the southwest,. Here we have ignored the strong, relatively narrow emission at -56 km s^{-1} , which is seen in DCN, but which is far less evident in H^{13}CN . The velocity gradient is larger in DCN than in H^{13}CN , which could result from the higher angular resolution in DCN compared to H^{13}CN .

3.4.3. $\text{CH}_3\text{CN } J = 12 \rightarrow 11$

In this section we discuss the structure, kinematics, opacity and temperature of CH_3CN . We show that although there is CH_3CN emission from the accretion disk, emission from the outflow dominates and hence prevents CH_3CN from being a good disk tracer for NGC 7538 S.

The emission from $\text{CH}_3\text{CN } J = 12 \rightarrow 11$ is confined to the immediate vicinity of NGC 7538 S (Figure 16). The emission is well resolved and shows an elliptical source centered at $0''.2 \pm 0''.03$, $-0''.4 \pm 0''.1$, relative to our nominal position for NGC 7538 S, i.e. slightly south of the stellar position. At $K = 0$, which has an excitation energy of 68.9 K above ground, the size of the CH_3CN emission is $\sim 4''.9 \times 1''.5$ with a p.a. of 70° . The emitting region gets progressively smaller for higher K levels, suggesting that the gas is hotter closer to the star. At $K = 3$, which has an excitation energy of 132.9 K, the size

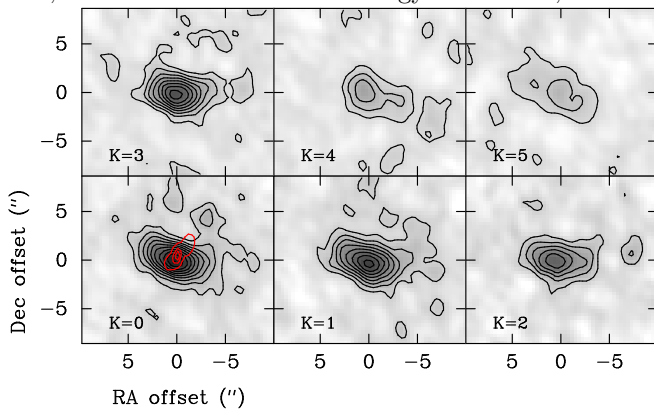


FIG. 16.— BIMA contour images of integrated $\text{CH}_3\text{CN } J = 12 \rightarrow 11$ for K-levels 0 to 5. For each K-level we have integrated the line emission over a 4.2 km s^{-1} wide velocity interval, except for K=4 and 5, where we have used a wider velocity interval, 5.3 km s^{-1} . The offsets are relative to $\alpha_{2000.0} = 23^{\text{h}} 13^{\text{m}} 44^{\text{s}}.98$, $\delta_{2000.0} = +61^\circ 26' 49''.5$, which is $0''.3$ to the south of the protostar. The beam FWHM is $2''.76 \times 2''.36$ PA 22.9° .

TABLE 5
LINE PARAMETERS FOR $\text{CH}_3\text{CN } J=12 \rightarrow 11$ TOWARDS
THE CENTER OF THE ACCRETION DISK

K level	V_{LSR} [km s^{-1}]	ΔV [km s^{-1}]	$\int T_{\text{MB}} dV$ [K km s^{-1}]
HPBW = $2.76 \times 2.36^{\text{a}}$			
0	$-56.4 \pm 0.1^{\text{b}}$	5.35 ± 0.17	16.6 ± 0.9
1	11.6 ± 0.8
2	9.4 ± 0.8
3	12.0 ± 0.9
HPBW = $3.16 \times 2.42^{\text{a}}$			
4	-56.9 ± 0.5	6.2 ± 1.3	5.4 ± 0.9
5	-55.3 ± 1.3	7.3 ± 4.1	4.3 ± 1.6
6	-56.6 ± 0.4	1.8 ± 1.2	1.1 ± 0.4
$\text{CH}_3^{13}\text{CN}$			
2	-56.3 ± 1.6	7.5 ± 3.5	2.7 ± 1.1
3	-55.8 ± 0.6	2.8 ± 1.2	1.2 ± 0.5

^a Image containing K-levels 0 to 3 have better uv-coverage than images containing K levels 4, 5, and 6, and the K = 2 and 3 transitions of $\text{CH}_3^{13}\text{CN}$. The latter data set has instrumental problems causing the data to be excessively noisy.

^b CLASS fit by keeping velocity separations between K-levels to their theoretical values and forcing the line width to be the same for all transitions.

of the emitting region $4''.0 \times 1''.5$ with a p.a. of 84° . At higher K-levels the emission is faint and the source size more uncertain, but appears to follow the same trend seen for lower K-levels, i.e. the emission becomes more compact and we see a gradual increase in the position angle. It would therefore appear that CH_3CN traces the accretion disk, although at low K-levels the position angle of the emission differs from what we observe in dust continuum and H^{13}CN . At higher K-levels the CH_3CN emission becomes even more misaligned, which we would not expect to observe if the emission originates in the accretion disk, unless the inner disk is warped relative to the colder, more extended disk. As we will see below, the CH_3CN emission is dominated by the outflow.

In Figure 18 we plot the integrated red- and blue-shifted emission of the K = 1 and 3 transitions and overlay them on the integrated emission from the line core of these lines, shows that the CH_3CN emission is dominated by the outflow. This is even more striking for the K = 3 transition, where the blue- and red-shifted line emission is well separated and aligned with the outflow. The cut along the disk-plane (Figure 19), however, shows only a marginal velocity gradient over the disk, yet, as we already seen, both $\text{H}^{13}\text{CN } J=1 \rightarrow 0$ and DCN $J=3 \rightarrow 2$ show a strong velocity gradient over the disk. Although this is somewhat surprising, it does not contradict our earlier results. CH_3CN is strongly dominated by the outflow, which may mask the emission from the accretion disk.

It is also possible that the CH_3CN emission is optically thick, which will make it difficult to see rotation of the disk. CH_3CN spectra towards the center of NGC 7538 S are shown in Figure 17. We detected all the K transitions, K = 0 to 6, and the K = 2 and 3 transitions of $\text{CH}_3^{13}\text{CN}$, which were included in our frequency setting (Table 2). In Table 5 we give results from Gaussian fits to the spectra presented in Figure 17. We fitted the

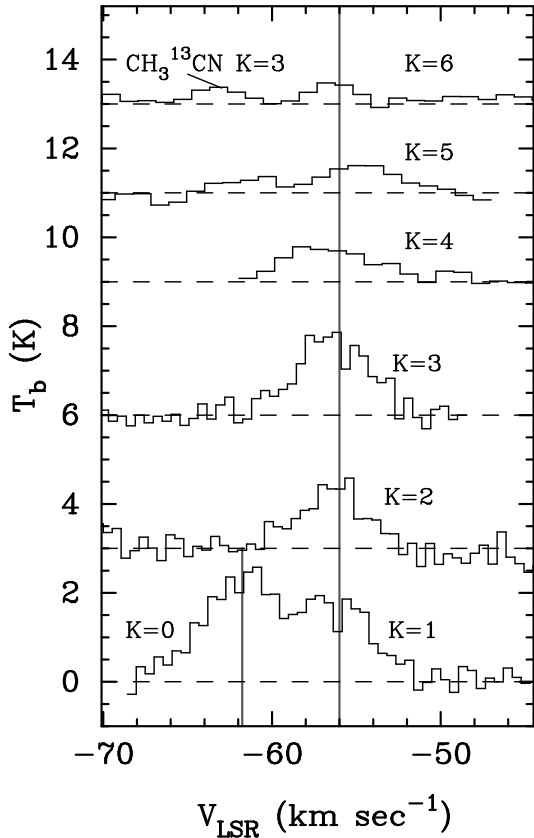


FIG. 17.— Observed $\text{CH}_3^{13}\text{CN } J = 12 \rightarrow 11$ spectra towards the center of NGC 7538 S for $K = 0$ to 6. The grey vertical line indicates the systemic velocity of the protostellar disk. The $K = 0$ and $K = 1$ spectra are blended, which is seen in the bottom spectra. The velocity corresponds to the $K = 1$ level, but we have also indicated with a grey line where the systemic velocity falls for the $K = 0$ line. The top spectrum includes the $\text{CH}_3^{13}\text{CN } K = 3$ line, which is separately labeled in the panel. The peak ratio of CH_3CN to $\text{CH}_3^{13}\text{CN}$ for $K = 3$ is $\sim 3 - 10$, indicating that the line is optically thick. Self absorption at the systemic velocity of the cloud or at slightly red-shifted velocities is seen in K -levels 0 to 3.

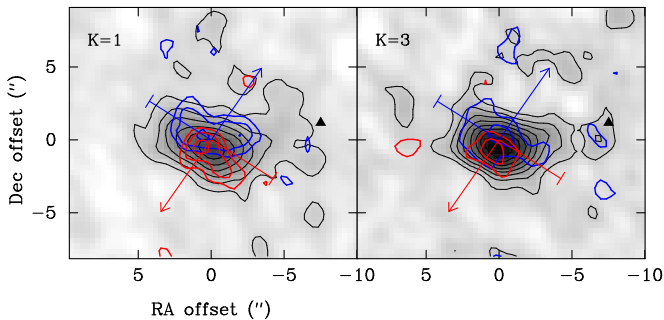


FIG. 18.— Greyscale plots enhanced with contours of integrated $\text{CH}_3^{13}\text{CN } J = 12 \rightarrow 11$ $K = 1$ emission (left panel) and $K = 3$ emission (right panel). Both $K = 1$ and $K = 3$ are integrated over 4.2 m s^{-1} as in Fig. 16. These contour plots are overlaid with contours of integrated high velocity emission, plotted in blue and red for the blue-shifted and red-shifted wings of the emission. The integrated blue- and red-shifted emission is aligned along the outflow direction (p.a. $\sim 145^\circ$), demonstrating that CH_3CN is tracing the outflow, not the disk.

$K = 0$ to 3 levels simultaneously by keeping the separation between the K components to their theoretical value, but allowed the FWHM to be a free parameter and constrained to be the same for all these K values.

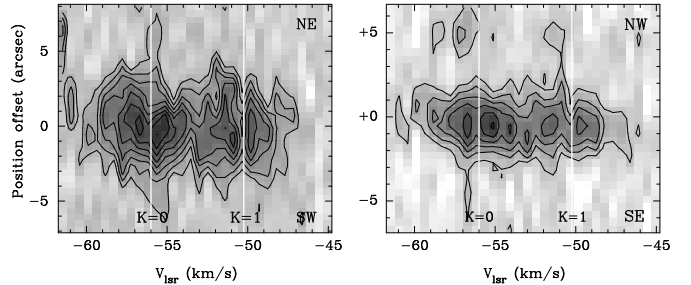


FIG. 19.— Position velocity cuts of $\text{CH}_3^{13}\text{CN } J = 12 \rightarrow 11$ $K = 0$ and $K = 1$ emission along the disk plane (left panel) and along the outflow (right panel).

The K -levels 4 to 6 were fitted individually. It is clear from these fits that the line widths get broader for increasing K -value, which is what one would expect, since these lines probe the hot outflow. The line profiles are not well fitted with a single Gaussian, because they have a broader underlying pedestal from the outflow. If we fit the $K = 3$ transition with a two-component Gaussian, we find that the integrated intensity of the broader component, $\Delta v = 9.3 \text{ km s}^{-1}$, is almost twice the value of the narrow (disk-)component. There is also a hint of a narrow self-absorption feature in the $K = 0$ to $K = 3$ transitions (Figure 17), suggesting that there is cold, somewhat optically thick CH_3CN gas in the surrounding cloud core. This self-absorption is also seen in the position velocity plots (Figure 19), confirming that it is real and not an artifact. Narrow self-absorption is also seen in the $K = 3$ transition, but slightly more red-shifted.

Since we detected emission from the $K = 2$ and 3 transitions of $\text{CH}_3^{13}\text{CN}$, we can use the line ratios to check whether CH_3CN is optically thin or thick. The ratios of the integrated $\text{CH}_3\text{CN}/\text{CH}_3^{13}\text{CN}$ line intensities are about 3 - 10, which strongly suggests that the CH_3CN lines are optically thick. Although CH_3CN is often optically thin in hot, dense molecular cloud cores, see e.g. Araya et al. (2005), it is not uncommon to find optically thick CH_3CN , especially in high-mass star forming regions (Pankonin et al. 2001; Watson et al. 2002; Remijan et al. 2004; Beltrán et al. 2005), when they are observed with high spatial resolution.

CH_3CN is traditionally analyzed using a rotational temperature equilibrium (RTE) analysis (Loren & Mundy 1984; Araya et al. 2005, and references therein). However, we know that some of the K -transitions are optically thick and that the source size changes as a function of K -level. Furthermore, we also know that we have some contribution from both the disk and the outflow, especially at low K -levels. An RTE or population-diagram analysis assumes that the gas is optically thin and in LTE at a single temperature, none of which is strictly true in this case. Nevertheless, it is instructive to look at the results of such an analysis. Since Araya et al. (2005) have done a recent in depth discussion of population-diagram analysis for CH_3CN , there is no reason for us to repeat any of the discussion here. Following Araya et al. (2005) we do a least squares fit linear fit of the equation

$$\ln(Z) = \ln\left(\frac{N_{\text{CH}_3\text{CN}}}{Q(T_{\text{rot}})}\right) - \frac{E_{JK}}{kT_{\text{rot}}}$$

where $Z = \frac{N_{JK}}{g_{JK}}$. To minimize the effect from the change

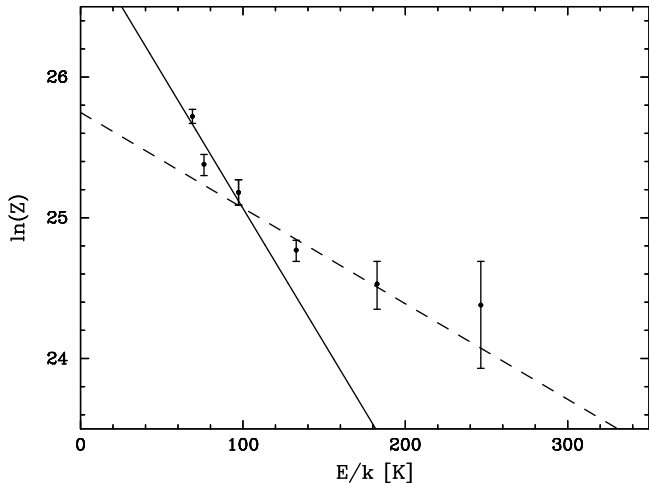


FIG. 20.— Population diagram of CH_3CN $J=12 \rightarrow 11$ towards NGC 7538 S, see discussion in Section 3.4.3. The solid curve shows a least squares fit to the three lowest K -transition, $K = 0$ to $K = 2$, while the dashed line is a fit for $K = 2$ to 5. The low K -transitions, $K = 0$ to 2, for which the emission is likely to include a non-negligible contribution from the accretion disk, correspond to a temperature of ~ 50 K, while the high K -transitions, which are dominated by the outflow, correspond to a temperature of 150 K.

in source size, we use the measured antenna temperatures for the peak position of CH_3CN ignoring any difference due to coupling of the source, except for a small correction for the $K = 4$ and $K = 5$ levels, which were imaged with a slightly different beam size (Table 5). Here we took the square of the ratio of the beam size, resulting in a correction factor of 0.83. The results of this analysis is shown in Figure 20. The population-diagram indicates that the CH_3CN emission cannot be characterized with a single rotational temperature. We have therefore separately done a least squares fit to the three lowest K -transitions, $K = 0$ to 2, for which the emission is likely to include a non-negligible contribution from the accretion disk, and for $K = 2$ to 5, for which we seen that the outflow is dominates. The fit to the low K -transitions give $T_{rot} = 52 \pm 10$ K, while the high K -transitions give $T_{rot} = 147 \pm 40$ K. Neither of these temperatures are very accurate. The low K -transitions are definitely optically thick, which will lead to an overestimate of the rotational temperature. Contribution from the outflow will also raise the temperature. The temperature of the disk is certainly less than 50 K and higher than 25 K, the temperature of the surrounding cloud core, since we see some self-absorption from virtually every molecule tracing the disk. The temperature of the outflow is not well constrained by our observations, because we have poor signal-to-noise at high K -levels, which could more accurately constrain the temperature of the outflow. However, analysis of the two H_2CO transitions $3_{03} \rightarrow 2_{02}$ and $3_{22} \rightarrow 2_{21}$, which are dominated by the outflow, also indicate a temperature of ≥ 100 K, in good agreement with what we derive from CH_3CN . Kalenskii et al. (2000), who did single dish observations of NGC 7538 S in the $J=6 \rightarrow 5$ and $J=5 \rightarrow 4$ transitions of CH_3CN with a beam size of $\sim 40''$, derived a rotation temperature of ~ 40 K, much lower than what we observe. They also measure a different radial velocity, -55.4 km s^{-1} , while we find a radial velocity of $\sim -56.3 \text{ km s}^{-1}$ (Table 5). Since their beam covers most of the cold cloud core surrounding

NGC 7538 S, it appears that the CH_3CN emission they observe is dominated by the cloud core, which we filter out in our BIMA observations.

4. DISCUSSION

4.1. Is NGC 7538 S surrounded by a rotating accretion disk?

NGC 7538 S powers a highly collimated thermal jet and drives a very young, hot molecular outflow, suggesting that it must be surrounded by a rotating accretion disk. We have shown that the star is embedded in a compact elliptical cloud core, which is approximately perpendicular to the thermal jet and the associated molecular outflow. High angular resolution observations tracers like H^{13}CN $J=1 \rightarrow 0$, HN^{13}C $J=1 \rightarrow 0$, H^{13}CO^+ $J=1 \rightarrow 0$, and DCN $J=3 \rightarrow 2$, which all are largely optically thin, show blue-shifted line emission to the northeast of NGC 7538 S and red-shifted to the southwest, with the highest velocities towards the center of the protostar. Such a velocity signature is characteristic for a rotating Keplerian disk. However, some of the velocity broadening seen towards the center of the protostar might be caused by the outflow powered by the disk, instead of originating in the faster rotating inner part of the disk. We therefore have to review our observational results with caution. We know that the outflow is much hotter than the bulk of the gas in the disk. It therefore tends to dominate the emission even for molecules, which are normally believed to be good disk tracers like CH_3CN (Cesaroni et al. 1997, 2005; Beltrán et al. 2004, 2005; Patel et al. 2005; Furuya et al. 2008). In Section 3.4.3 we show that for NGC 7538 S the CH_3CN emission originates from the dense outflow gas near the surface of the disk, where the outflow is launched. The emission from CH_3CN therefore appears roughly orthogonal to the outflow.

Based on our discovery of a Keplerian like rotation in NGC 7538 S using H^{13}CN $J=1 \rightarrow 0$ (Sandell, Wright & Forster 2003), we thought that DCN might work equally well and would provide us higher spatial resolution, if we observed the $J=3 \rightarrow 2$ transition at 1.4 mm. However, as we saw in Section 3.4.2, the DCN $J=3 \rightarrow 2$ transition is clearly affected by the outflow. Even though it also traces the dense gas in the disk, the relatively strong emission from the outflow makes it difficult to reliably separate the outflow emission from that of the disk. For estimating a Keplerian mass, we therefore only use the results from H^{13}CN $J=1 \rightarrow 0$, because H^{13}CN appears least affected by the outflow, and therefore provides the best information about the kinematics of the neutral gas surrounding NGC 7538 S. However, because NGC 7538 S is surrounded by a very dense cold cloud core, all our high density tracers, including H^{13}CN , are affected by self-absorption. Most of this self-absorption is likely to originate in cold dense gas in the surrounding cloud envelope, but some of it could also originate in the colder outer portions of the disk, because the self-absorption becomes much more prominent at the center of the disk at the highest spatial resolutions. Since the self-absorption is slightly red-shifted (Figure 11, right panel), and almost certainly dominated by the accretion flow towards the central protostar, it makes the line emission appear more blue-shifted. Southwest of NGC 7538 S there is also an extended cloud component roughly at the systemic ve-

locity of the cloud, see Section 3.4.2 and Figure 13. This emission blends in with the red-shifted emission from the rotating disk, which together with an unknown amount of red-shifted self-absorption results in uncertain velocities in the red-shifted side of the disk.

Despite these difficulties, our new observations clearly confirm a velocity gradient in the dense gas disk surrounding NGC 7538 S. Position velocity plots of H^{13}CN $J=1 \rightarrow 0$ and DCN $J=3 \rightarrow 2$ show a roughly Keplerian like rotation curve centered on the protostar with a diameter of $\lesssim 5''$ (14,000 AU). If we assume that the disk is rotationally supported and take the velocities derived from H^{13}CN , we derive an enclosed mass of $\sim 14 M_{\odot}$, uncorrected for inclination. The inclination angle of the disk is $\sim 50^{\circ}$. Therefore the enclosed mass of the disk and the central protostar is $\sim 24 M_{\odot}$. We do not have a mass estimate for the central protostar, but based on the bolometric luminosity, $\sim 10^4 L_{\odot}$, it is probably has a mass of $\sim 10 M_{\odot}$, or about the same order as the mass of the disk. Such massive disks can be self-regulated at a condition of marginal Jeans stability and still appear to have an approximately Keplerian rotation curve (Bertin & Lodato 1999).

Cesaroni et al. (2007) argue that disks like the one Sandell, Wright & Forster (2003) discovered around NGC 7538 S should be called toroids rather than disks. They further argue that such toroids may simply be transient structures, which may or may not evolve into a “classical” Keplerian disk. In this follow-up study we show that the Keplerian disk surrounding NGC 7538 S, is much smaller than previously thought and it is therefore not a transient structure. In high-mass protostars, the extreme accretion rates of $\geq 10^{-4} M_{\odot} \text{ yr}^{-1}$, and the high pressure from the surrounding cloud, may enable such a “disk” to survive long enough to form an O-star. In this respect, NGC 7538 S, could well be a younger analogue of NGC 7538 IRS 1, which by all accounts still appears to be surrounded by an accretion disk (Sandell et al. 2009). In the case of IRS 1, which has a luminosity of an O7 star, but which is still heavily accreting, the disk has probably evolved into a more “classical” thin disk, which is rather hard to image, because the free-free emission from the central O-star is much brighter than the disk at mm-wavelengths, which is the only wavelength regime, where we have arrays with sufficient spatial resolution to potentially resolve and image such a disk.

4.2. *Is NGC 7538 S a high-mass star?*

Our observations confirm that NGC 7538 S lies in the center of a cold, massive cloud core with a diameter ~ 1 pc, and a mass $2,000 M_{\odot}$ (Section 3.1), which therefore provides the necessary conditions for the formation of high-mass stars, i.e. essentially the whole core has a surface density, $\Sigma \gtrsim 1 \text{ g cm}^{-2}$ (McKee & Tan 2002; Krumholz & McKee 2008). NGC 7538 S coincides within errors with a cold far-infrared source with a luminosity $\sim 1.5 \cdot 10^4 L_{\odot}$ (Werner et al. 1979; Thronson & Harper 1979), suggesting an early B-star, if it is a single star. IRS 11, the only near-IR source in the vicinity of NGC 7538 S, can only account for about a tenth of this luminosity, and the same is true for the small cluster of Spitzer 8 μm sources surrounding IRS 11 (Paper II). Therefore the bulk of the luminosity appears to be generated in the very massive elliptical cloud core (~ 100

M_{\odot}) cloud core, in which NGC 7538 S is embedded. Here NGC 7538 S completely dominates the luminosity. It drives a highly collimated thermal jet (Paper II), powers a massive, very young bipolar outflow (Sandell, Wright & Forster 2003), and excites OH, CH_3OH (Class II), and H_2O masers (Argon et al. 2000; Pestalozzi et al. 2006; Kameya et al. 1990). OH 1665-MHz masers are only found in young massive star forming regions (Caswell 1998; Argon et al. 2000), mostly associated with Ultra Compact H II regions. The same is true for Class II CH_3OH masers (Minier et al. 2003), i.e. no CH_3OH maser have yet been found toward a low or intermediate mass star. Although CH_3OH masers sometimes are associated with OH masers, the majority of them are found in weak or radio quiet regions. They are therefore believed to trace a younger, perhaps protostellar phase, in the evolution of high-mass stars (Caswell 1998; Ellingsen 2006). The observed accretion rate for the disk surrounding NGC 7538 S is $\sim 1 \cdot 10^{-3} M_{\odot} \text{ yr}^{-1}$. Such accretion rates have not been seen in low or intermediate mass protostars, but accretion rates in the range $10^{-3} - 10^{-4} M_{\odot} \text{ yr}^{-1}$ are commonly inferred for young high-mass stars of comparable luminosity (Molinari et al. 1998; Cesaroni et al. 1999; Beuther et al. 2002b; Beuther, Schilke & Stanke 2003; Fontani et al. 2004). Accretion rates as high as a few times $10^{-2} M_{\odot} \text{ yr}^{-1}$ have been reported (Beltrán et al. 2004, 2005), although such high accretion rates are generally only seen towards high luminosity UC H II regions (Hofner, Petersen & Cesaroni 2003; Zapata et al. 2008). Theoretical models of collapsing clouds show that the accretion rates increase rapidly in the beginning of the collapse phase and decrease monotonically later on (Li 1998; Yorke & Sonnhalter 2002), which may be why the observed accretion rate is on the high side for a region which has a total luminosity of $\sim 1.5 \cdot 10^4 L_{\odot}$. Since NGC 7538 S has the luminosity of a high-mass star and excites OH and CH_3OH Class II maser emission, which has only been seen in high-mass stars, it must be a high-mass star.

5. SUMMARY AND CONCLUSIONS

We have carried out extensive observations of the star forming core NGC 7538 S with BIMA in mostly optically thin tracers with spatial resolutions ranging from $\sim 3''$ to $8''$. Additionally we have acquired complementary observations with FCRAO and JCMT to fill in lacking short spacing in our BIMA observations, which are needed to improve the image fidelity and reliability of our images of molecules like HCO^+ , H_2CO , and H^{13}CN , which are spatially very extended.

We confirm that there is a very young high-mass (proto)star in the compact elliptical core, which has a size of $8'' \times 3''$ and a mass of 85 - 115 M_{\odot} . Recent sub-arcsecond continuum imaging at 110 and 224 GHz with CARMA (Paper II) resolve the elliptical core into three compact sources, all of which are almost certainly protostars. The strongest one of the three sources agrees within $0''.15$ with the adopted position for the high-mass protostar, which is $\sim 2''$ to the northeast from the center of the compact elliptical core. The protostar is seen as a faint, extremely obscured mid-IR source, which coincides with a VLA thermal jet, and an OH and a CH_3OH class II methanol maser. The star is surrounded by a massive, rotating accretion disk, which drives a highly collimated

thermal jet and powers a very compact, hot molecular outflow. We see clear evidence for accretion towards the protostar. Almost all molecular transitions that we have observed, show red-shifted self-absorption, which can be explained only by infall motions of the gas in front of the protostar. The accretion signature is very strong in the optically thick HCO^+ $J=1 \rightarrow 0$ transition, which shows infall velocities up to $\sim 15 \text{ km s}^{-1}$. We have used this accretion profile to derive a direct estimate of the accretion rate towards the disk, and find an accretion rate $\sim 10^{-3} M_{\odot} \text{ yr}^{-1}$. We also estimated the accretion rate by assuming that the accretion rate is about three times the outflow rate, and by assuming a steady state infall to the disk, with an infall velocity equal to the observed rotation velocity of the disk at the radius R . All three methods give very similar results. Such high accretion rates are sufficient to quench the formation of an H II region and allow the central protostar to continue to grow in mass (Walmsley 1995; Keto 2003, 2007).

The rotating accretion disk is best seen in H^{13}CN $J=1 \rightarrow 0$. H^{13}CN is only marginally affected by emission from the intense hot outflow, while the emission from the outflow may dominate or severely hinder us from seeing the disk in many of the molecular transitions that we have observed. We found that DCN $J=3 \rightarrow 2$, which we expected to be an equally good disk traces as H^{13}CN , is strongly affected by the outflow. Due to the high angular resolution, $\sim 2''.6$ (Table 2), we can separate most of

the outflow emission from the disk-emission and therefore confirm that NGC 7538 S is surrounded by a rotating accretion disk. The emission from methylcyanide, CH_3CN , however, is largely optically thick and the higher K-levels are completely dominated by the hot outflow emission near the surface of the disk.

BIMA observations of H^{13}CN $J=1 \rightarrow 0$ supplemented with FCRAO data show that the cloud core, in which NGC 7538 S is embedded, has a radius of $\sim 0.5 \text{ pc}$, and a mass $\sim 2000 M_{\odot}$. The size and mass of the core agrees very well with what we derive from analysis of the SCUBA 850 and $450 \mu\text{m}$ data presented by Sandell & Sievers (2004), while the mass estimate from a single dish C^{18}O $J=2 \rightarrow 1$ map is much lower, suggesting that CO is depleted (frozen onto grains) in the cold cloud envelope. The cloud core is dense and massive enough to provide the necessary conditions for high-mass star formation.

The BIMA array was operated by the Universities of California (Berkeley), Illinois, and Maryland with support from the National Science Foundation. We want to thank Dr. W. M. Goss for helpful comments and support throughout this project. Special thanks goes to Dr. Mark Heyer, who did the FCRAO observations for us, and to the JCMT telescope system specialists, who did all the JCMT observing in service mode. We thank the anonymous referee for an extremely careful reading of our manuscript, which considerably improved our paper.

REFERENCES

- Allen, A., Li, Z.-Y., & Shu, F. H. 2003, *ApJ*, 599, 363
 Araya, E., Hofner, P., Kurtz, S., Bronfman, L., & DeDeo, S. 2005, *ApJS*, 157, 279
 Argon, A. L., Reid, M. J., & Menten, K. M. 2000, *ApJS*, 129, 159
 Beltrán, M. T., Cesaroni, R., Neri, R., Codella, C., Furuya, R. S., Testi, L., & Olmi, L. 2004, *ApJ*, 601, L187
 Beltrán, M. T., Cesaroni, R., Neri, R., Codella, C., Furuya, R. S., Testi, L., & Olmi, L. 2005, *A&A*, 435, 901
 Beuther, H., Schilke, P., Menten, K. M., Motte, F., M., Shridharan, T. K., & Wyrowski, F. 2002a, *ApJ*, 566, 945
 Beuther, H., Schilke, P., Sridharan, T. K., Menten, K. M., Walmsley, C. M., & Wyrowski, F. 2002b, *A&A*, 383, 892
 Beuther, H., Schilke, P., & Stanke, T. 2003, *A&A*, 408, 601
 Bertin, G., & Lodato, G. 1999, *A&A*, 350, 694
 Blake, G. A., Sutton, E. C., Masson, C. R., & Phillips, T. G. 1987, *ApJ*, 315, 621
 Bonnell, I. A., & Bate, M. R. 2006, *MNRAS*, 370, 488
 Bontemps, S., André, P., Terebey, S., & Cabrit, S. 1996, *A&A*, 311, 858
 Brown, D. W., & Chandler, C. J. 1999, *MNRAS*, 303, 855
 Cabrit, S., & Bertout, C. 1990, *ApJ*, 348, 530
 Caswell, J. L. 1998, *MNRAS*, 297, 215
 Cesaroni, R., Felli, M., Jenness, T., Neri, R., Olmi, L., Robberto, M., Testi, L., & Walmsley, C. M. 1999, *A&A*, 345, 949
 Cesaroni, R., Felli, M., Testi, L., Walmsley, C. M., & Olmi, L. 1997, *A&A*, 325, 725
 Cesaroni, R., Neri, R., Olmi, L., Testi, L., Walmsley, C. M., & Hofner, P. 2005, *A&A*, 434, 1039
 Cesaroni, R., Galli, D., Lodato, D., Walmsley, C. M., & Zhang, Q. 2007, in *Protostars and Planets V*, Eds. B. Reipurth, D. Jewitt, and K. Keil, (University of Arizona Press:Tucson), p. 197
 Chandler, C. J., Brogan, C. L., Shirley, Y. L., & Loinard, L. 2005, *ApJ*, 632, 371
 Choi, M., Evans II, N.J., & Jaffe, D.T. 1993, *ApJ*, 417, 624
 Clarke, C. J., & Bonnell, I. A. 2008, *MNRAS*, 388, 1171
 Corder, S. 2008, Ph.D. thesis, California University of Technology
 Davis, C.J., Moriarty-Schieven, G., Eisloffel, J., Hoare, M. G., & Ray, T.P. 1998, *AJ*, 115, 1118
 Ellingsen, S. P. 2006, *ApJ*, 638, 241
 Fontani, F., Cesaroni, R., Testi, L., Molinari, R., Zhang, Q., & Walmsley, C. M. 2004, *A&A*, 424, 179
 Furuya, R. S., Cesaroni, R., Takahashi, S., Codella, C., Momose, M., & Beltrán, M. T. 2008, *ApJ*, 673, 363
 Hildebrand, R. H. 1983, *QJRAS*, 24, 267
 Hogerheijde, M. R., van Dishoeck, E. F., Blake, G. A., & van Langevelde, H. J. 1998, *ApJ*, 502, 315
 Hofner, P., Petersen, S., & Cesaroni, R. 2003, *ApJ*, 514, 899
 Jørgensen, J. K. 2004, *A&A*, 424, 589
 Kalenskii, S. V., Promislov, V. G., Alakoz, A. V., Winnberg, A., & Johansson, L. E. B. 2000, *A&A*, 354, 1036
 Kameya, O., Morita, K. -I., Kawabe, R., & Ishiguro, M. 1990, *ApJ*, 355, 562
 Keto, E. 2003, *ApJ*, 599, 1196
 Keto, E. 2007, *ApJ*, 666, 976
 Krumholz, M. R., McKee, C. F. 2008, *Nature*, 451, 1082
 Lada, C. J., & Harvey, P. M. 1981, *ApJ*, 245, 58
 Li, Z.-Y. 1998, *ApJ*, 493, 230
 Loren, R. B., & Mundy, L. G. 1984, *ApJ*, 286, 232
 Maeder, A., & Behrend, R. 2002, *Ap&SS*, 281, 75
 Mangum, J., & Wootten, A. 1993, *ApJS*, 89, 123
 Mannings, V., & Sargent, A. I. 1997, *ApJ*, 490, 792
 Manoj, P., Ho, P. T. P., Ohashi, N., Zhang, Q., Hasegawa, T., Chen, H.-R., Bhatt, H. C., & Ashok, N. M. 2007, *ApJ*, 667, L187
 McKee, C. F., & Tan, J. C. 2002, *Nature*, 416, 59
 Minier, V., Booth, R. S., & Conway, J. E. 1998, *A&A*, 336, L5
 Minier, V., Ellingsen, S. P., Norris, R. P., & Booth, R. S. 2003, *A&A*, 403, 1095
 Mitchell, G. F., Maillard, J.-P., Allen, M., Beer, R., & Belcourt, K. 1990, *ApJ*, 363, 554
 Molinari, S., Testi, L., Brand, J., Cesaroni, R., & Palla, F. 1998, *ApJ*, 505, L39
 Moscadelli, L., Reid, M. J., Menten, K. M., Brunthaler, A., Zheng, X. W., & Xu, Y. 2009, *ApJ*, 693, 406
 Najita, J., Carr, J. S., & Mathieu, R. D. 2003, *ApJ*, 589, 931
 Norberg, P., & Maeder, A. 2000, *A&A*, 359, 1025

- Pankonin, V., Churchwell, E., Watson, C., & Biegging, J. H. 2001, *ApJ*, 558, 194
- Patel, N. A., Curiel, S., Sridharan, T. K., Zhang, Q., Hunter, T. R., Ho, P. T. P., Toremles, J. M., Moran, J. M., Gómez, J. F., & Anglada, G. 2005, *Nature*, 437, 109
- Pestalozzi, M. R., Minier, V., Motte, F., & Conway, J. E. 2006, *A&A*, 448, L57
- Remijan, A., Sutton, E. C., Snyder, L. E., Friedel, D. N., Liu, S.-Y., & Pei, C.-C. 2004, *ApJ*, 606, 917
- Sandell, G., Goss, W. M., & Wright, M. 2005, *ApJ*, 621, 839
- Sandell, G., Goss, W. M., Wright, M., & Corder, S. 2009, *ApJ*, 699, L31
- Sandell, G., & Sievers, A. 2004, *ApJ*, 600, 269
- Sandell, G., Wright, M., & Forster, J. R. 2003, *ApJ*, 590, L45
- Sault, R. J., Teuben, P. J., and Wright, M. C. H. 1995, in *ASP Conf. Ser. 77: Astronomical Data Analysis Software and Systems IV*, Eds. R.A. Shaw, H.E. Payne, and J.J.E. Hayes (Astronomical Society of the Pacific: San Francisco), p. 433
- Schreyer, K., Henning, Th., van der Tak, F. F. S., Boonman, A. M. S., & van Dishoeck, E. F. 2006, *ApJ*, 637, L129
- Shepherd, D. S., & Churchwell, E. 1996, *ApJ*, 472, 225
- Shepherd, D. S., Yu, K. C., Bally, J., & Testi, L. 2000, *ApJ*, 535, 833
- Shu, F. H., Allen, A., Shang, H., Ostriker, E., & Li, Z.-Y. 1999, in *The Origins of Planetary Systems*, Eds. C. J. Lada, and N. D. Kylafis (Kluwer Academic Publishers: Dordrecht), p. 193
- Simon, M., Dutrey, A., & Guilloteau, S. 2000, *ApJ*, 545, 1034
- Snell, R. L., Scoville, N. Z., Sanders, D. B., & Erickson, N. R. 1984, *ApJ*, 284, 176
- Stahler, S., Palla, F., & Ho, P. T. P. 2000, in *Protostars and Planets IV*, Eds. V. Mannings, A. P. Boss, & S. S. Russell (University of Arizona Press: Tucson), p. 327
- Thronson, H. A., Jr., & Harper, D. A. 1979, *ApJ*, 230, 133
- Tomisaka, K., *ApJ*, 502, L163
- Tuthill, P. G., Monnier, J. D., Danchi, W. C., Hale, D. D. S., & Townes, C. H. 2002, *ApJ*, 577, 826
- Walmsley, M. 1995, *Rev. Mex. AA Ser. Conf.*, 1, 137
- Watson, C., Churchwell, E., Pankonin, V., & Biegging, J. H. 2002, *ApJ*, 577, 260
- Werner, M. W., Becklin, E. E., Gatley, I., Matthews, K., Neugebauer, G., & Wynn-Williams, C.G. 1979, *MNRAS*, 188, 463
- Weintraub, J., Moran, J. M., Wilner, D. J., Young, K. H., Rao, R., & Shinnaga, H. 2008, *ApJ*, 677, 1140
- Wilking, B. A., Blackwell, J. H., & Mundy, L. G. 1990, *AJ*, 100, 758
- Wolfire, M. G., & Cassinelli, J. P. 1987, *ApJ*, 319, 850
- Yorke, H. W., & Sonnhalter, C. 2002, *ApJ*, 569, 846
- Zapata, L. A., Palau, A., Ho, P. T. P., Schilke, P., Garrod, R. T., Rodríguez, L. F., & Menten, K. 2008, *A&A*, 479, L25
- Zhang, Q., Hunter, T. R., Brand, J., Sridharan, T. K., Cesaroni, R., Molinari, S., Wang, J., & Kramer, M. 2005, *ApJ*, 625, 864
- Zhang, Q., Hunter, T. R., Brand, J., Sridharan, T. K., Molinari, S., Kramer, M. A., & Cesaroni, R. 2001, *ApJ*, 552, L167
- Zhang, Q., Hunter, T. R., & Sridharan, T. K. 1998, *ApJ*, 505, L151
- Zheng, X.-W., Zhang, Q., Ho, P. T. P., & Pratap, P. 2001, *ApJ*, 550, 301